Title
History and Drivers of Slow Landslide Movement at Oak Ridge Earthflow, California

Author
Nereson, Alexander Lewis

Publication Date
2018

Peer reviewed|Thesis/dissertation

UNIVERSITY OF CALIFORNIA
SANTA CRUZ

HISTORY AND DRIVERS OF SLOW LANDSLIDE MOVEMENT AT OAK RIDGE EARTHFLOW, CALIFORNIA

A dissertation submitted in partial satisfaction
of the requirements for the degree of

DOCTOR OF PHILOSOPHY

in

EARTH SCIENCES

by

Alexander L. Nereson

December 2018

The Dissertation of Alexander Nereson is approved:

_____
Associate Professor Noah Finnegan, Chair

_____
Professor Andrew Fisher

_____
Kevin Schmidt, Ph.D.

_____
Lori Kletzer
Vice Provost and Dean of Graduate Studies

Table of Contents

List of Figures

List of Tables

Abstract

History and drivers of slow landslide movement at Oak Ridge earthflow, California

Alexander L. Nereson

The persistent movement of deep-seated, slow-moving landslides is a common phenomenon with important scientific and practical implications. These landslides, often referred to as earthflows, can dominate erosion in mountainous landscapes, control the long-term evolution of catchment geometry, and cause progressive damage to infrastructure and property over time. The role of earthflows in shaping landscapes is amplified by their longevity. Historical observations demonstrate that they are commonly active for decades or centuries, while geologic and geochronologic evidence further suggests that some may persist in intermittently-active states for millennia. Slow, persistent motion over these timescales requires complementary mechanisms to both repeatedly reactivate previously failed materials and to limit velocity during periods of activity. More than 30 years of robust scientific investigations into the nature of these mechanisms has yielded tremendous insights. These include the sensitivity of earthflows to rainfall-driven changes in pore-water pressure, the existence of internal feedbacks that limit earthflow velocity after the onset of motion, and the recognition that external factors, like climate and base-level, help set the periodicity of intermittent earthflow movement. A common goal of all these investigations has been to generate

data and models that will allow for the prediction of future earthflow behavior, which remains challenging despite many advances. Predicting the velocity of slow landslides over multi-decadal timescales requires an understanding of the potential drivers of earthflow motion, analytical frameworks and models to connect those drivers to kinematic response, and historical records of movement with sufficient spatial and temporal resolution to test model predictions. Predicting velocity on shorter timescales, such as the onset of motion in a given wet season, requires high-temporal resolution, time-series measurements of the hydro-mechanical properties of the earthflow in question. And lastly, scaling up predictions of future velocity at one earthflow to many will require the use of high-spatial resolution, remotely-sensed imagery capable of monitoring large regions with repeat measurements. This dissertation aims to contribute to each of these requirements through an extended study of Oak Ridge earthflow, a long-lived, slow-moving landslide in California's northern Diablo Range. In Chapter 1, we used a time series of aerial imagery to assemble an 80-year kinematic history for Oak Ridge earthflow. We find that spatial patterns of earthflow velocity were controlled largely by the slope of the underlying failure plane, whereas temporal patterns were governed largely by climate-driven changes in surface moisture balance (PDSI) at the annual-decadal scale. Declines in sediment supply acted as a secondary control on temporal velocity variations over our study period, however, the influence of this driver likely grows at longer timescales. In Chapter 2, we use 10 years of high-spatial resolution, multispectral satellite imagery to assess the long-accepted, but relatively untested, hypothesis that hydro-mechanical isolation of earthflows from

surrounding, stable slopes contributes to their ability to fail persistently over time. In Chapter 3, we use of 2.5 years of high-temporal resolution records of rainfall, pore-water pressure, and displacement to argue that the initial onset of earthflow acceleration in response to seasonal rainfall is likely to be more closely related to the timescales of vadose zone processes than pore-water pressure diffusion through saturated soil, as has been previously suggested. Collectively, these studies provide new observations and approaches towards understanding earthflow behavior at multiple scales.

For my parents, Diane and Brent.

Acknowledgements

This dissertation could not have been completed without the support of many friends, family, and colleagues who helped me personally and scientifically. Foremost, I must thank my dissertation advisor, Noah Finnegan, for accepting me to the PhD program (twice!), for providing me with the opportunity to build a research program from the ground up, and for his constant encouragement over the past six years. I hope to emulate his positivity, inquisitiveness, and humility in all my future work.

I would also like to thank the other members of my thesis committee: Andy Fisher and Kevin Schmidt. Andy was a seemingly limitless source of field, laboratory, logistical, and technical support. Kevin graciously offered much of his time to lend insightful comments and propose promising leads for future research questions. I would also like to thank Slawek Tulacyzk, who served on my Qualifying Exam committee and helped shape the nature of my research questions at the earliest stages.

My gratitude extends also to the Finnegan research lab, which has been a reliable source of inspiration, knowledge, and friendship over the years. Thank you to Jon Perkins, Kerri Johnson, Danica Roth, Claire Masteller, Allison Pfeiffer, Colleen Murphy, Luca Malatesta, Rachael Klier, and Dave Santaniello. To Claire, a dear friend since our very first visit to campus seven(!) years ago, I am deeply grateful that you where there to lean on, learn from, and laugh with through this process.

Several other colleagues have contributed significantly to this document. Thank you to Selina Davila Olivera, a co-author of Chapter 2, for your help in the field and laboratory. Thanks also to Andy Fisher, Walker Weir, Dom Vanden Dries, Tali Babila,

Rob Franks, Colin Carney, and Brandon Cheney for their lab and logistical support with Chapter 2. Thanks also to Jon Perkins for helpful discussions and ideas that made Chapter 3 possible. Field assistance for all three chapters was provided by many people, including Erika Martinelli, Colleen Murphy, Earl O'Bannon, Grace Barcheck, Allison Pfeiffer, John Perkins, Danica Roth, Neil Foley, Mikey Nayak, John Sandru, John Galetzka, Dylan Schmeelk, Brandon Cheney, and Andrew Racz.

Generous funding and/or support for these projects was provided by the National Science Foundation, the UCSC Earth and Planetary Sciences Department, the Northern California Geological Society, UNAVCO, the Nevada Geodetic Laboratory, and Planet Labs. Thank you also to our partners at the San Francisco Public Utilities Commission and to Russ Fields for access to Oak Ridge earthflow.

Given that my fascination with geology started during my first year at Macalester College, I would be remiss not to thank my mentors from Minnesota. During my years at Mac, Karl Wirth was my professor (of my very first college course, among several others thereafter), my academic and research advisor, my personal mentor, and a second father figure to me (as he was to many other students in his 2006 Dynamic Earth course!). It would be impossible to overstate my gratitude for his instruction, guidance, encouragement, and critical feedback. I must also thank Kelly MacGregor. It was during her Environmental Geology course, while standing knee-deep in the Sunrise River, that I first felt like a scientist. Kelly's infectious positivity and enthusiasm for geology, learning, and life in-general still serves as a wellspring of inspiration to me. And without Kelly (also a UCSC alum), I would have never heard of Santa Cruz, let

alone have had the great fortune to study here. Lastly, I must thank Jeff Thole, whose creative use of both sarcasm and the Socratic method (sometimes simultaneously!) was a surprisingly effective teaching strategy in both the classroom and the laboratory. Thanks to Jeff, every scenic hike I take in Minnesota is now ruined because I can't take my eyes of the ground as I scan it for agates.

Finally, there are many family and friends whose support has carried me through this thesis. Thank you to Alexandra, Neil, Naor, and Jenna. To my mom and dad, thank you for your love, encouragement, and perspective. Academia can be a weird place for first-generation college students, and I don't think any of us knew what we were getting into when we were applying to universities back in 2005. Thanks for always being there and having my back. To my partner Andrew, thank you for all the love, patience, diversions, and adventures over the past five years. I cannot wait to see what our future holds.

Chapter 1.

Drivers of earthflow motion revealed by an 80 yr record of displacement from Oak Ridge earthflow, Diablo Range, California, USA

Previously published as:

Nereson, A.L. and Finnegan N.J. (2018) Drivers of earthflow motion revealed by an 80 yr record of displacement from Oak Ridge earthflow, Diablo Range, California, USA, Geological Society of America Bulletin, doi: https://doi.org/10.1130/B32020.1

1.1 Abstract

Predicting the velocity of slow landslides over multidecadal time scales requires an understanding of the potential drivers of landslide motion, analytical frameworks or models that connect those drivers to kinematic response, and historical records of movement that have sufficient spatial and temporal resolution to test model predictions. Given that detailed long-term records of slow landslide movement are still relatively uncommon, we used a time series of aerial imagery to assemble an 80 yr (1937–2017) record of movement for the Oak Ridge earthflow, a slow-moving

landslide in California's northern Diablo Range. Landslide movement was unsteady and nonuniform during this period. We used this history of movement, visual evidence from imagery and the field, and a record of surface moisture balance (the Palmer Drought Severity Index) to evaluate the relative roles of possible drivers of movement. Drivers considered included: supply of mobile regolith from the landslide source zone, fluvial debuttressing from below, changes in climate forcing over time, and changes in failure plane orientation in space. Specifically, we found that spatial patterns of earthflow velocity within the transport zone, where the bulk of movement occurred, were controlled largely by the slope of the underlying failure plane, whereas temporal patterns were governed largely by climate-driven in surface moisture balance (PDSI) at the annual-decadal scale. Declines in sediment supply acted as a secondary control on temporal velocity variations over our study period; however, the influence of this driver likely grows at longer time scales. Evidence for transient waves of motion in response to fluvial debuttressing was limited to the toe, and continued monitoring of Oak Ridge earthflow is required to determine whether those perturbations in sediment flux will migrate further upslope.

1.2 Introduction

1.2.1 Earthflows

The importance of landslides as natural hazards and as drivers of landscape evolution in mountainous areas is well documented. Large landslides that fail unexpectedly and accelerate rapidly are likely to cause loss of life (Petley, 2012),

catastrophic damage to property (Fleming and Taylor, 1980), and abrupt changes in catchment geometry and sediment flux to stream channels (Korup et al., 2010). By comparison, slow-moving landslides are unlikely to cause human casualties, but they can nevertheless result in extensive property damage (e.g., Bertolini et al., 2005) and have outsized impacts on erosion and sediment budgets (Kelsey, 1978; Mackey and Roering, 2011; Simoni et al., 2013).

Earthflows are a common type of slow-moving landslide characterized by a flow-like appearance and persistence over decades to centuries (Hungr et al., 2014). They form above fine-grained bedrock in plastic, clayey soil; are commonly large (>500 m long) and deep (>5 m); and move at rates less than ~10 m/yr (Baum et al., 2003). Active earthflows frequently extend from ridge tops to valley bottoms (Mackey and Roering, 2011) and are classically described as having an "hourglass" planform outline, with a bowl-shaped source area, an elongate transport zone, and a lobate toe (Keefer and Johnson, 1983). The surfaces of earthflows show signs of pervasive disruption, including hummocky topography with undrained depressions, boulder-strewn slopes, tension cracks, and systems of ephemeral gullies in which the drainage pattern can change substantially from year to year (Kelsey, 1978).

Earthflows tend to occur in areas with weak rocks, strongly seasonal precipitation, and moderate to steep slopes (Keefer and Johnson, 1983). Even within small geographic areas, they tend to cluster spatially based on various environmental factors such as aspect, weathering rates, vegetation type, and proximity to fault-induced damage zones, as summarized by Scheingross et al. (2013).

Notwithstanding their name and appearance, most earthflow movement approximates rigid block sliding along discrete basal and lateral shear surfaces. Evidence for sliding as the dominant mode of movement (>75%) comes from vertical displacement profiles (e.g., Keefer and Johnson, 1983; Vulliet and Hutter, 1988; Zhang et al., 1991; Simoni et al., 2013) and from observations of earthflow boundaries, which are frequently marked by sharp lateral ridges and slickensided strike-slip faults (Keefer and Johnson, 1983; Fleming and Johnson, 1989). During periods of steady movement, a relatively small component of surface velocity comes from distributed internal deformation, but it is thought to be more prevalent during short bursts of acceleration, or "surges," when internal strains rates are particularly high (Hungr et al., 2014).

1.2.2 Drivers of Earthflow Motion

The drivers of earthflow movement are known to vary in time and space. For example, earthflows commonly exhibit annual cycles of activity that are related to the onset of seasonal precipitation, which acts to increase pore-fluid pressure and decrease effective stress within slopes (e.g., Kelsey, 1978; Keefer and Johnson, 1983; Iverson and Major, 1987; Hilley et al., 2004; Handwerger et al., 2013). Deep-seated earthflows often exhibit lag times of several weeks between the onset of seasonal precipitation and acceleration as the soil moistens and pore pressure waves associated with groundwater flow propagate toward the basal shear zone (Iverson and Major,

1987; Handwerger et al., 2013). For earthflows that maintain near-saturated conditions year-round, however, basal pore pressures may always be sufficient to sustain motion (Baum and Reid, 2000). In these cases, even small pressure perturbations, such as those associated with atmospheric tides or precipitation during individual thunderstorms are known to cause rapid changes in velocity (Coe et al., 2003; Schulz et al., 2009a).

The controls on the movement of earthflows over long periods of time (10^1–10^4 yr), which are more relevant to landscape evolution (as opposed to hazards), are less well constrained. This is due, in part, to a relative lack of long-term records of motion, but also to the fact that multiple factors likely govern the motion of earthflows on decadal time scales. First, Mackey and Roering (2011) argued that weathering rates and the conversion of bedrock to mobile regolith high up on hillslopes may be the ultimate control on the periodicity of earthflow movement. Where they are active, earthflows transport sediment at rates far in excess of what can be supplied by background erosion rates (Mackey and Roering, 2011). Consequently, it is possible that earthflows exhaust their supply of mobile regolith and cease motion, resuming only after a reservoir of weathered hillslope sediment has been reestablished.

Mackey et al. (2009) also noted that the influence of sediment supply on landslide motion may be modulated by climate-driven changes in pore-fluid pressure. Other workers have also linked cycles of earthflow movement to long-term precipitation variability and have shown earthflow velocity to be correlated with indices of surface

soil moisture balance over periods of 12–71 yr (Coe, 2012; Bennett et al., 2016b). In particular, exceptional drought conditions have been shown to coincide with a sustained decrease in the average velocity of earthflows in northern California's Eel River catchment (Bennett et al., 2016b). Droughts may also have a secondary effect of "priming" earthflow-prone slopes for future surges by promoting the growth of soil desiccation cracks, which allow rapid infiltration of rainfall when wet conditions resume (McSaveney and Griffiths, 1987).

Finally, there is strong evidence for earthflow activity that is triggered when hillslopes are debuttressed from below by river incision (e.g., McKean, 1993; Bilderback et al., 2014). The clustering of landslides above steep knickpoints in river channels (Bennett et al., 2016a) and in areas of relatively high catchment relief (Scheingross et al., 2013) also demonstrates the role of base-level forcing on earthflow activity.

These specific drivers for landslide failure are not mutually exclusive and individually influence the key factors governing earthflow stability for a given friction angle: landslide depth, slope, and pore-fluid pressure (e.g., Lambe and Whitman, 1969). Specifically, transient changes in landslide depth and slope may be modulated by sediment supply, which can either increase or decrease driving shear stresses via tributary slope failures that deposit material onto the surface of active earthflows (e.g., Iverson, 1986b) or through progressive regolith starvation (e.g., Mackey and Roering, 2011). Landslide slope may also be modulated by river incision, which can increase the topographic gradient and hence driving stresses at

landslide toes. Alternatively, aggradation in river valleys can buttress and stabilize landslide toes. Finally, landslide pore-fluid pressure is directly modulated by shallow groundwater pressures and hence is intimately tied to seasonal precipitation totals (e.g., Iverson and Major, 1987). Iverson (1986a, 1986b) presented a model for slow landslide failure that directly incorporated the transient effects of base-level forcing, sediment supply, and pore-fluid pressure in driving transient waves of motion along slow landslides.

At a single earthflow, movement tends to vary in space as well as time. The emergence of distinct kinematic zones, each with their own styles and rates of deformation, is a common observation of earthflow behavior (e.g., Fleming et al., 1999; Mackey et al., 2009; Guerriero et al., 2014). However, linking such space-time variability in landslide motion to these specific drivers is challenging because data having sufficient spatial and temporal resolution are unusual. Consequently, the extent to which slow landslide motion is dominated by transient perturbations versus steady motion is typically not known. For example, do spatial patterns of velocity reflect migrating kinematic waves or simply spatial variation in the underlying failure slope or landslide depth? Similarly, is temporal variation in velocity driven by upslope-propagating (or downslope-propagating) kinematic waves or by year-to-year soil moisture balance? Prediction and mitigation of the effects of slow landslides require not only an analytical framework that can incorporate the diverse drivers of landslide motion (e.g., Iverson, 1986a, 1986b), but also data sets that can be used to assess nonuniform, unsteady landslide motion in light of these drivers.

To this end, we present an 80 yr record (1937–2017) of movement for Oak Ridge earthflow (Fig. 1), an active, slow-moving landslide in California's northern Diablo Range, as measured from historical aerial imagery. We also developed a simple model, which we used to estimate surface velocity solely as a function of long-term surface moisture balance within each of the earthflow's five main kinematic zones. To the extent that measured and modeled velocities are well correlated with one another, we attribute movement primarily to climate-driven changes in surface moisture balance. For those kinematic zones or periods of time in which measured and modeled velocities are not well correlated with one another, we used observational evidence from aerial images and field visits to explore the relative roles of base level, sediment supply, and topographic slope (which may all vary in space or time) as drivers of slow landslide motion over decadal time scales.

1.3 Study Area

1.3.1 Diablo Range, Northern California

The Diablo Range is a northwest-striking member of the central California Coast Ranges that extends for nearly 200 km and lies just inland of the Santa Cruz and Santa Lucia Mountains. The topography of the northern Diablo Range alternates between rolling plateaus and deep canyons (up to 900 m). Like much of California, it has a Mediterranean climate with hot, dry summers and cool, wet winters, but it receives less overall precipitation than mountains to the west (Kauffman, 2003). In

the northern Diablo Range, bedrock consists largely of the Franciscan Complex, an assemblage of variably deformed and metamorphosed rock units formed in a subduction zone during the Mesozoic and early Cenozoic Eras (Wakabayashi, 1992). With widespread occurrence throughout the state, Franciscan lithologies include primarily detrital sedimentary rocks such as sandstones and argillaceous mélanges that are well known for their low strength and high susceptibility to slope failure. Many documented instances of earthflows in California occur within these units (Kelsey, 1978; Keefer and Johnson, 1983; Iverson and Major, 1987; Scheingross et al., 2013; Roering et al., 2015).

1.3.1 Oak Ridge Earthflow

Oak Ridge earthflow is a seasonally active earthflow located in the northern Diablo Range, 20 km northeast of San Jose, California (Fig. 1A). Positioned on the south-facing flank of Oak Ridge, it extends 1.8 km (area = 0.35 km^2) in the horizontal direction from ridge top to valley bottom, spans nearly 600 m of vertical relief, and has an average slope of 17°. Oak Ridge earthflow appears to be the only measurably active earthflow in the Arroyo Hondo catchment, despite the fact that dormant earthflows cover ~4% of the total surface area (Nereson et al., 2013). Scattered outcrops indicate that bedrock geology consists primarily of Franciscan sandstone and mudstone mélange, and soil texture ranges from silt to sandy loam, with gravel and coarse clasts up to 10+ m in diameter at the surface (Davila Olivera et al., 2017).

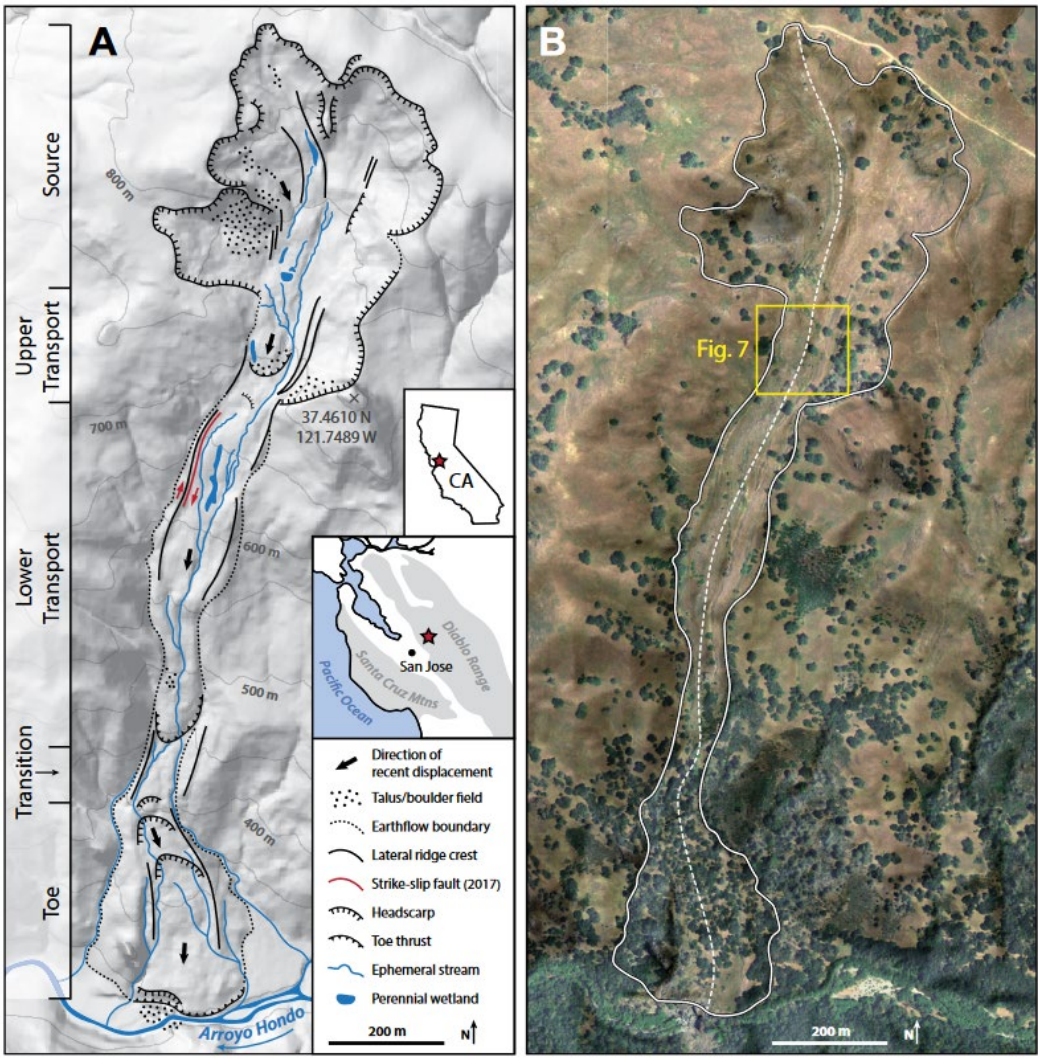

Figure 1.1. (A) Shaded relief map of Oak Ridge earthflow, with prominent geomorphic features depicted. Spatial extents of the five morpho-kinematic units described in the text are shown at left. Recent displacement vectors were determined from historical aerial imagery and 2015–2017 field observations. Active strike-strike slip fault was observed and surveyed June 2017. Insets show location of study area in California (CA). (B) 2012 aerial image from U.S. Department of Agriculture National Agriculture Imagery Program (NAIP). Solid white line delimits extent of Oak Ridge earthflow; dashed white line indicates location of elevation transect shown in Figure 3A; extent of Figure 7 is shown in yellow.

Average annual precipitation is 52.7 cm (20.7 in.) and falls almost exclusively as rain between the months of October and April (PRISM Climate Group, 2017). This supports a mix of open oak savanna (~70% coverage) with some oak woodland

(25%) at lower elevations (Fig. 1B). Aside from periodic grazing and a small, spring-fed pond maintained for cattle, the earthflow and surrounding stable slopes are largely undisturbed by human development.

Oak Ridge earthflow exhibits many of the hallmarks of classic earthflow topography. Its hummocky surface (Fig. 2A), with >5 m of local relief, stands in contrast to the smooth, convex surfaces of adjacent stable slopes. Sets of nested lateral ridges several meters high bound the earthflow in its narrower sections (Fig. 2B), and strike-slip faults with well-formed slickenlines are located just inboard of and parallel to the ridges (Figs. 1A and 2C). During the wet season, numerous internally drained depressions retain water for periods of days to months, and ephemeral streams incise dendritic networks of rills and gullies (Fig. 2A). Groundwater-fed perennial wetlands are also present (Fig. 1A) and seem to be resilient features, even through dry spells. We observed standing water and marshy patches of vegetation in autumn 2015, at the end of a dry season that capped off an exceptional multiyear drought in California (Griffin and Anchukaitis, 2014).

Oak Ridge earthflow is a “complex” landslide in the sense that there is evidence for multiple styles of slope failure and multiple episodes of activity that have resulted in stacked earthflow deposits. We divided Oak Ridge earthflow into several distinct morphologic units, including the source zone, transport zone, “transition” zone, and extensional zone, or toe (Fig. 1A). Starting at the top, Oak Ridge earthflow taps a broad (400-m-wide), amphitheater-shaped source zone composed of several individual alcoves, each with their own steep headscarp. These alcoves appear to have

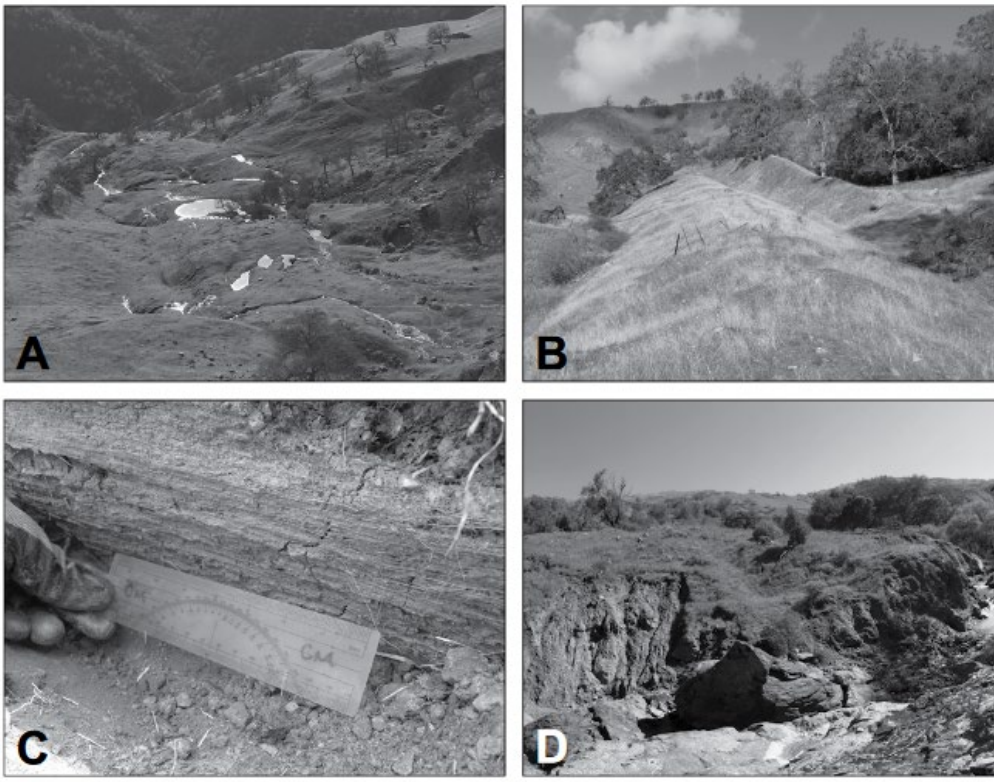

Figure 1.2. (A) Photo showing abundance of pools and streams that are present during the wet test months of the year. View looking down onto the source and upper transport zones in January 2016. Diameter of largest pond is 23 m. (B) Pair of nested lateral ridges, each with ~5 m of vertical relief. View looking uphill from the upper transport zone in November 2016. (C) Slickenlines on an east-dipping strike-slip fault mark the active western boundary of the earthflow in June 2017 (see Fig. 1A for fault trace). Appearance of slickenlines is enhanced by grass roots aligned in the direction of slip, toward the right. (D) View looking northeast at the interface between the earthflow toe and the channel of Arroyo Hondo. This interface is actively cut by stream erosion and is highly susceptible to shallow mass movements that occasionally deliver large boulders to the channel (foreground). Diameter of largest boulder in foreground is 27 m.

delivered material to the transport zone by a combination of rotational and translational slides, rock avalanches, and debris flows. Only the western alcoves appear to have been recently active, given differences in topographic roughness and crosscutting relationships with lateral ridges at their bases (Fig. 1A).

The narrow transport zone is ~100 m wide and begins at an elevation of ~800 m (Fig. 1A), where it is surrounded on three sides by source-zone alcoves. From there, it

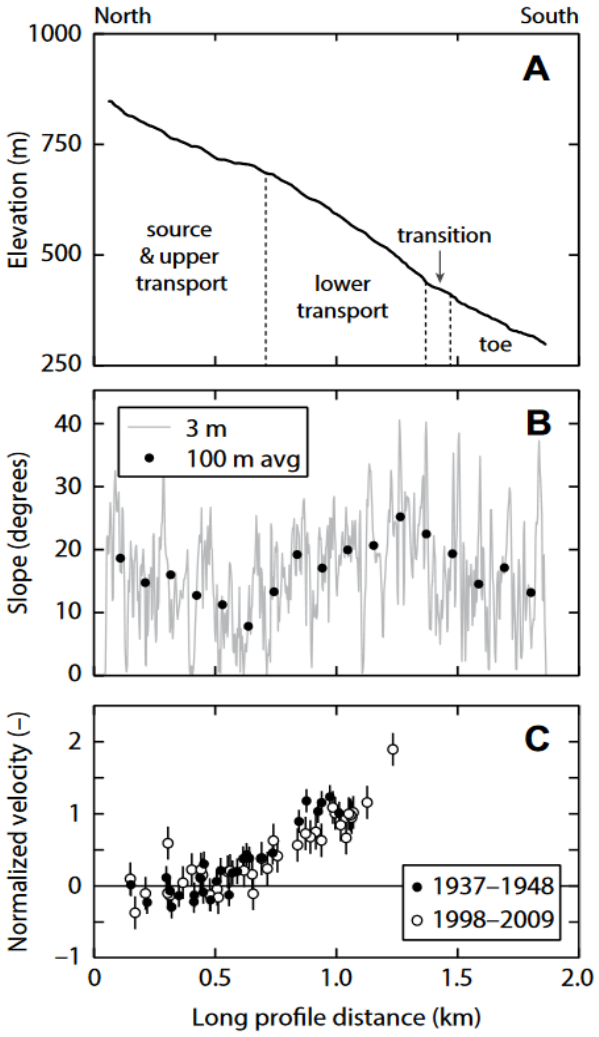

Figure 1.3. Longitudinal profiles of (A) earthflow elevation, (B) surface slope, and (C) normalized velocities for 1937–1948 and 1998–2009. Elevation values were sampled along the dashed transect in Figure 1B and projected onto a north-south axis. In the lower transport zone, an increase in average surface slope by ~10° is associated with an order of magnitude increase in ground control point (GCP) velocity over the same distance (B and C). Elevation data are from U.S. Geological Survey (1/9 arcsecond 3D Elevation Program [3DEP] data, collected in 2006).

extends south for ~1000 m, where it terminates at a small, lobate toe, perched midslope, at an elevation of 450 m. Sharp lateral ridges flank the sides of the transport zone in many places, and it is incised down the middle by a large axial gully. The average surface gradient of the transport zone increases by over 10° (Fig. 3B) in the downslope direction, creating a pronounced convexity in the earthflow's longitudinal profile (Fig. 3A).

At the base of the transport zone, there is a relatively narrow (60 m) and low-gradient "transition" zone that extends longitudinally for 100 m (Fig. 3A). The transition zone is also composed of earthflow deposits and flanked

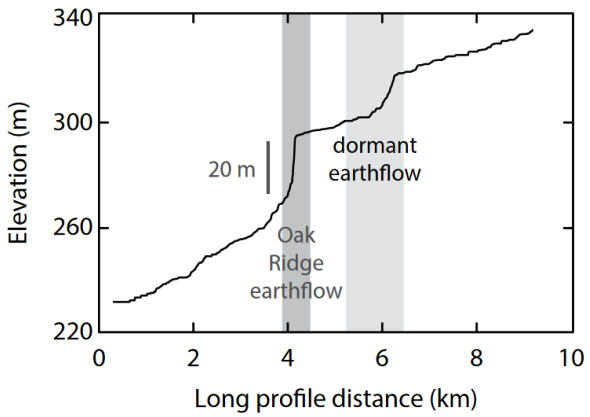

Figure 1.4. Longitudinal profile of Arroyo Hondo, centered on the reach where Oak Ridge earthflow and another, unnamed earthflow enter the stream channel. This reach features large knickpoints ≥20 m high that are characterized in the field by boulder dams and cascades several meters tall.

by lateral ridges, but it is positioned stratigraphically below the material of the transport zone. Its surface appears less disturbed, and therefore potentially less active than the transport zone.

Last, the toe region of the Oak Ridge earthflow complex consists of a fan-shaped deposit (up to 275 m wide) that impinges on the floodplain and channel of Arroyo Hondo (Fig. 1A). Typically, earthflows form a compressional toe (Keefer and Johnson, 1983), where mobile regolith is stacked along progressive thrust faults during deposition. The toe of Oak Ridge earthflow was likely formed in this same manner; however, in its present state, it appears to be undergoing extension. Evidence for extension comes from the observation that the toe is marked by a series of three prominent scarps (at ~400 m elevation; Fig. 1A) with back-rotated hanging-wall blocks, each showing several meters of offset (up to 10 m). These failures are restricted to the middle 50% of the toe, creating what appears to be an active extensional zone that is ~90 m wide.

At the interface between the earthflow and Arroyo Hondo, there is a large outcrop that has been exposed through the combined effects of stream erosion and shallow mass movements (Fig. 2D). Along the base of this outcrop, there are multiple exposures of sub-horizontal basal shear surfaces with slickenlines oriented north-

south. Below the toe, an accumulation of large boulders that toppled from the earthflow interface forms a >20-m-high knickpoint in the long profile of Arroyo Hondo (Fig. 4). In this reach, the combined channel-floodplain width is as small as 10 m, but it widens by an order of magnitude just upstream, where a large amount of Arroyo Hondo sediment appears to be impounded by the boulder dam formed at the earthflow toe.

1.4 Methods

1.4.1 Remotely Sensed Imagery and Displacement Measurements

We used a time series of 22 high-resolution, georeferenced orthoimages to track the positions of features such as trees and rocks during an 80 yr period from 1937 to 2017. Orthoimages with variable spatial resolutions (0.5–2.0 m) were purchased or freely downloaded from several sources (Table DR1). To reduce the effects of systematic offsets between the images on our position measurements, we aligned all imagery to a recent aerial image in the series, a 0.6-m-resolution image that was acquired in 2016. We based our alignment on 23 stable ground control points (GCPs) that were distributed across the study area and were visible in all 21 images. We traced outlines around features used as stable GCPs and calculated centroids of the resultant polygons in ArcMap. For our image alignments, we used a first-order polynomial transformation in ArcMap, which allows for limited warping of rasters, and subsequently resampled the data using the cubic convolution method at each image's original spatial resolution. Georeferencing errors were evaluated using the

total root mean square error (RMSE) of the stable GCP residuals. Total RMSE values for each image's georeferencing are listed in Table DR1 (see footnote 1[1]).

In total, 55 unique features within the mapped boundaries of the earthflow were included in our analysis as mobile GCPs and tracked between aligned images (Fig. 5; see also Tables DR2 and DR3 for positions [footnote 1]). We chose these points based on several criteria. First, they needed to be visible in more than one image (vs. stable GCPs, which needed to be visible in all images). Next, we selected small trees or rocks with well-defined edges. This is because the centroids of large trees or groups of trees are difficult to identify from one image to another, especially with changes in sun and camera angles. Due to a number of possible factors (e.g., trees died, lost their leaves, or were buried by earthflow motion), only about half of all GCPs (n = 22) were visible in all 22 images, and these were primarily located in the upper transport zone and source zone of Oak Ridge earthflow. We made use of all 55 points, however, for calculating average velocity of morphologic units between each image pair.

Given that each image records a snapshot captured on a different day of the year and at a different time of day, the collection reflects variability in both sun angle and azimuth. The resulting shadows cast by the trees and rocks we used as GCPs therefore change the apparent shape of these features and make it more difficult to

[1] GSA Data Repository item 2018248, Tables DR1–DR4, is available at http://www.geosociety.org/datarepository /2018 or by request to editing@geosociety.org.

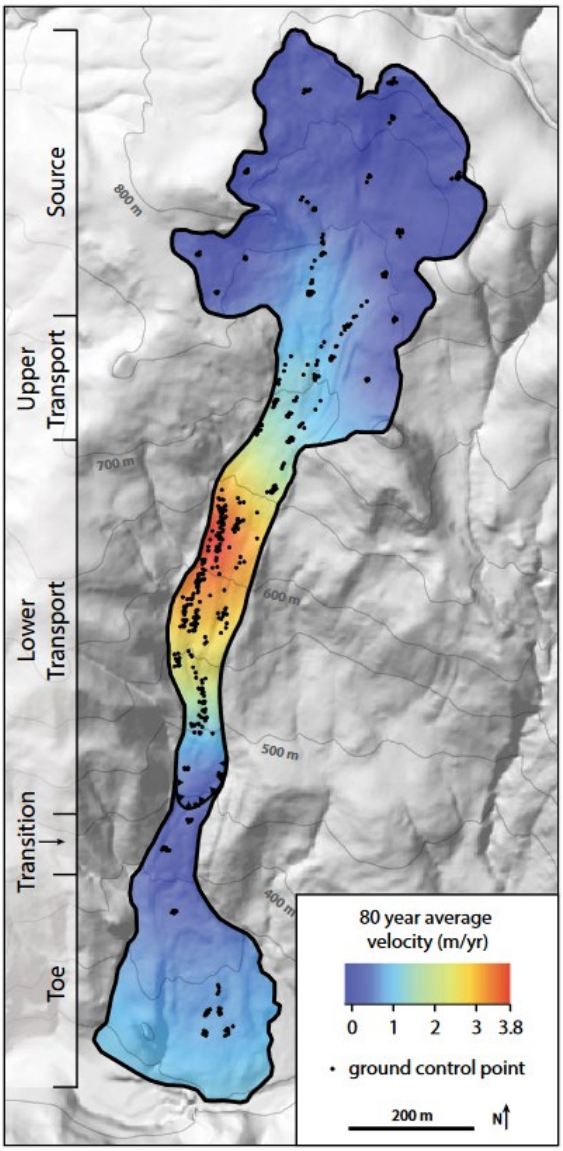

Figure 1.5. Average velocity map of Oak Ridge earthflow for the period 1937–2017. Twentyone interpolated velocity maps were created, one for each aerial image interval. Grid values from each map were summed and divided by 80 yr to calculate average velocity. The highest average velocity (3.8 m/yr) occurs in the lower transport zone. Black dots indicate the locations of all mobile ground control points used in this analysis. See Tables DR2 and DR3 for geographic coordinates (see text footnote 1). Black line with triangular teeth indicates the location of advancing front of the lower transport zone.

accurately locate the center of a GCP in a given year. This effect appears to be most pronounced in the east-west direction, in which a spurious sawtooth pattern of motion

was observed for some GCPs due to images captured either early or late in the day. This shadowing effect may also explain why some GCPs exhibited apparent nonphysical motion in the northward (upslope) direction, even after image alignment.

To minimize effects of shadows, we only used the north-south components of GCP displacement in the following analysis. These are reasonable (albeit, minimum) estimates for total GCP motion, given that Oak Ridge earthflow is oriented

primarily north-south. In the following, we refer to north-south displacement and north-south velocity simply as displacement and velocity.

1.4.2 Surface Moisture Balance

A major goal of this study was to assess the surface moisture balance at Oak Ridge earthflow and its controls on landslide motion. This built off the work of those who have successfully correlated indices of surface moisture with changes in earthflow velocity (e.g., Coe, 2012, Bennett et al., 2016b). Bennett et al. (2016b), for example, showed that the average velocity of 98 earthflows in northern California decreased in association with a long-term moisture deficit that began at the turn of the twenty-first century. As a metric of surface moisture balance for Oak Ridge earthflow, we use the Palmer Drought Severity Index (PDSI). The PDSI, also applied to earthflows by Bennett et al. (2016b), was designed to measure cumulative departures in surface water balance over time and is currently the most prominent index of meteorological drought in the United States (Dai et al., 2017). The National Oceanic and Atmospheric Administration (NOAA) regularly publishes PDSI values averaged over large regions called climate divisions. Because we are interested in the moisture balance at one particular location, however, we calculated a local PDSI for Oak Ridge earthflow using monthly precipitation totals and average temperature from the PRISM Climate Group. PRISM generates gridded estimates of these values using digital elevation models and measured weather data from individual ground stations (Daly et al., 2002). We downloaded an 87 yr time series (1930–2017) of PRISM

precipitation and temperature data from the 4 km grid cell centered over Oak Ridge earthflow (37.4563°N, 121.7564°W; PRISM Climate Group, 2017) and used the MATLAB code of Jacobi et al. (2013) to compute monthly PDSI. Additional inputs to the PDSI calculation were: latitude = 37.46°N and soil available water content = 1.5, which is within the range for loamy soils (USDA Natural Resources Conservation Service, 1998). The reference period was set to the full record of data downloaded from PRISM (1930–2017).

1.4.3 Sensitivity of Landslide Motion to Surface Moisture Balance

In order to assess the sensitivity of landslide motion to surface moisture balance, we began with an assumption that landslide velocity, for slow-moving landslides, tends to stabilize for a given pore-fluid pressure forcing. The reason(s) why catastrophic acceleration of slow landslides does not occur, although a topic of much interest in landslide mechanics, is(are) not addressed directly here. For our work, we assumed that some mechanism, such as dilatant strengthening (Iverson, 2005; Schulz et al., 2009b) or forced circulation around bed roughness elements (Baum and Johnson, 1993), acts as a negative feedback on unstable landslide acceleration and results in quasi-static frictional sliding that can persist or recur intermittently for months to years, as is observed widely for similar slow-moving landslides in California (e.g., Handwerger et al., 2013).

Because PDSI values may be both positive (wet) and negative (dry), we applied a constant offset to the PDSI data in order to make all values positive and then

normalized them by the full range of PDSI in our 80 yr record. The resulting normalized PDSI values ranged from zero, which represents the lowest PDSI in our record, to one, which represents the highest value. We used these normalized PDSI values to compute a power-law function of monthly PDSI:

$$Vmodeled = PDSI^{n}, \quad (1)$$

where *Vmodeled* is the modeled velocity, and *n* is an exponent ranging from 1 to 10. The results can be thought of as a time series of modeled monthly velocities and were subsequently normalized by the maximum value in the series, such that the maximum normalized velocity in each model output was 1, and the minimum was 0.

While we do not have a specific mechanistic rationale for the power-law relationship between velocity and PDSI, we used this function because it brackets a wide range of plausible end-member physical relationships between water balance and velocity. For example, $n = 1$ would indicate a linear relationship between surface water balance and velocity, but this is probably unrealistic, given that a threshold seems to control landslide motion at Oak Ridge. That is, measurable motion only appears to occur in a handful of particularly wet years. On the other hand, an extremely high exponent approximates rapid, catastrophic acceleration above a threshold, which is also unrealistic because of the relatively modest downslope displacement observed during wet winters at Oak Ridge.

To determine which power-law exponent resulted in the best-fit velocity model for our data, we calculated the RMSE between each power-law model output and the normalized average velocity record for each kinematic zone of the earthflow. The

power-law exponent that minimized RMSE between the measured and modeled velocity records was determined to be the best-fit exponent.

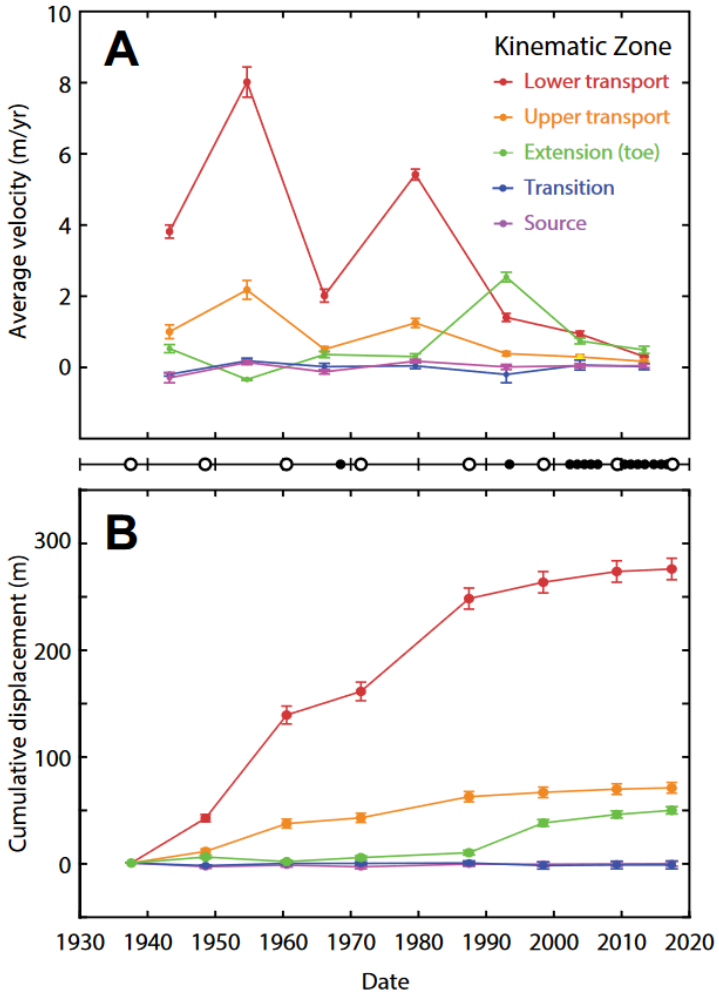

Figure 1.6. Average velocity and standard error for each kinematic unit. (B) Cumulative displacement for each kinematic unit with standard errors propagated. Average velocity in the transport zone varied substantially before the 1980s but decreased monotonically thereafter. Black dots along center number line indicate acquisition dates of all imagery used in this study; white dots indicate the images with approximately decadal spacings used to make this figure. Only some ground control points (GCPs) were visible in a given year, so the number of GCPs used to calculate the mean velocity for a given time interval changed for each interval. Cumulative displacement was calculated by integrating velocity over time.

1.5 Results

1.5.1 Historical Earthflow Displacement

Motion of Oak Ridge earthflow was unsteady and nonuniform over the period from 1937 to 2017. In general, measured velocities were highest in the transport zone, where 80 yr average rates exceeded 3 m/yr in places (Fig. 5). Even within this zone, however, velocity varied substantially in space and time, and we found that velocity typically increased from north to south within the transport zone during a given time interval. Figure 3C shows the normalized velocity of individual features from the source and transport zones for the periods 1937–1948 and 1998–2009. In both data series, a several-fold increase in velocity is apparent over a distance of ~1 km, with peak velocities measured near the advancing frontal lobe of the transport zone. Given this spatial gradient in velocity, we divided this morphologic unit into two kinematic zones: a slower-moving, upper transport zone (UTZ) and a faster-moving, lower transport zone (LTZ), which typically moved at rates two to four times faster than the UTZ, on average. Figure 6A shows that the relative velocities of the LTZ and UTZ with respect to each other were similar over time, but their magnitudes fluctuated greatly during the first half of our record. In the LTZ, for example, average velocity from 1948 to 1960 was 8.1 m/yr, whereas the average velocity from 1960 to 1971 was only 2.0 m/yr. Since the 1980s, the average transport zone velocity has consistently decreased (Fig. 6A). We integrated average velocity over time to calculate total cumulative displacements of 275.5 m in the LTZ and 70.5 m in the UTZ (Fig. 6B). Eighty-year average velocities were 3.4 and 0.9 m/yr, respectively.

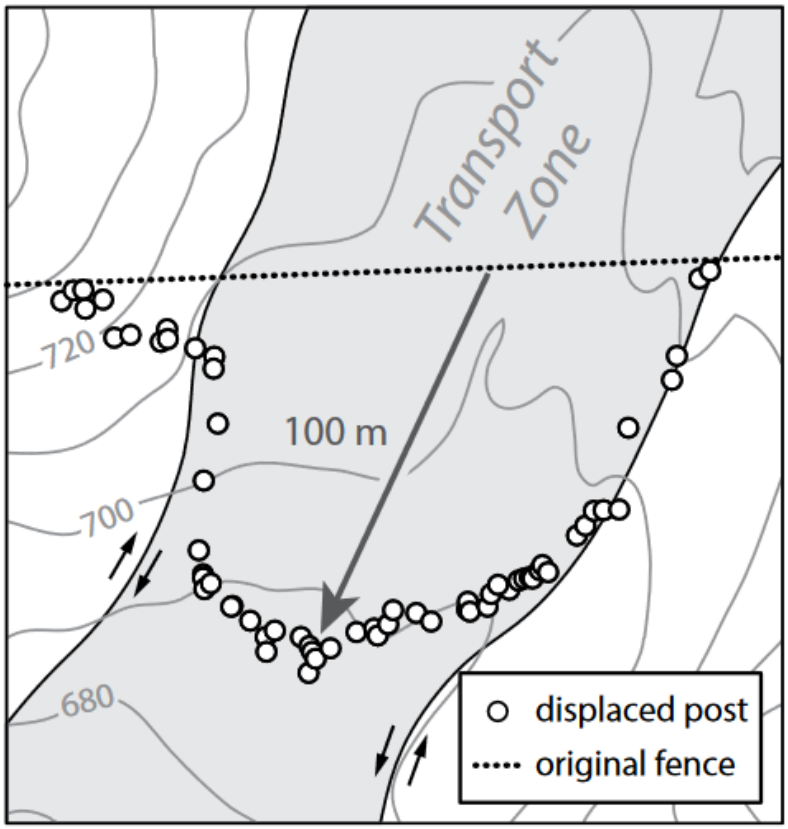

Figure 1.7. Map view displacement profile of derelict fence posts in the upper transport zone (shaded). Maximum displacement of ~100 m was observed in the center of the landslide; however, the majority (60%–70%) of displacement occurred near the lateral shear boundaries. Contour interval = 10 m. Locator map is shown in Figure 1B.

Figure 6A shows earthflow velocity over time within each kinematic zone, using a subset of images sampled at approximately decadal spacings (average interval = 11.4 yr). This sub-sampling emphasizes long-term trends at the expense of short-term variability from the past 15 yr, for which there is a higher temporal density of images, but relatively little movement. Movement that did occur in these recent years, however, was concentrated in 2005 and 2006, during which velocities in the LTZ were measured to be 5.5 and 6.5 m/yr on average, respectively. This brief period of acceleration underscores the fact that annual velocity can vary several-fold from one

year to another and that decadal averages may not be representative of earthflow movement that occurs in a relatively small number of years (e.g., 10 yr average LTZ velocity was 0.9 m/yr from 1998 to 2009).

In addition to the downslope variability in velocity, we also quantified the cross-slope variability in velocity within the UTZ using a derelict barbed wire fence that consists of wooden posts spaced every few meters. This fence line spans the width of the earthflow and has been progressively deformed along with the soil beneath it. Using a handheld global positioning system (GPS) unit, we collected the positions of fence posts and plotted the resulting displacement profile in Figure 7. This profile indicates a maximum displacement of ~100 m in the center of the earthflow, but the majority (60%–70%) of that displacement occurred in relatively narrow bands near the lateral edges of the earthflow. The construction date of the deformed fence is unknown to the authors, but we infer that the displacement profile outlined by the fence posts integrates at least 80 yr of motion based on the movement of nearby GCPs. This pattern is consistent with the widely reported conclusion that earthflows tend to move largely by sliding along narrow shear zones (or even strike-slip faults) with a relatively small component of distributed internal deformation (Keefer and Johnson, 1983; Vulliet and Hutter, 1988; Zhang et al., 1991; Simoni et al., 2013). Indeed, in the spring and summer of 2017, a strike-slip fault with fresh slickenlines formed along the western edge of the transport zone and extended continuously for at least 165 m (Fig. 1A), indicating a high degree of strain localization at the earthflow margins.

Above the transport zone, Oak Ridge earthflow's large source area was relatively immobile during the period of record. Imagery and recent field visits indicate that occasional rock falls and debris flows have delivered minor amounts of material from the steep headscarps onto the earthflow surface; however, coherent downslope motion was absent from all source alcoves, except for one in the northwest part of the source zone. There, GCP 12 moved a total of 31 m southeast in the years prior to 1987 (black arrow in source zone, Fig. 1A), but it moved relatively little thereafter. Field observations after the winter of 2017 confirm that this alcove may be reactivating, with ~1 m of vertical offset along a freshly ruptured headscarp. No other headscarps were active in the 2017 season.

The transition zone was stationary over the period of record (Fig. 6). Since 1937, however, it has been progressively buried from above by the advancing lobe of the LTZ. In the 1990s, it also began eroding from below, as the earthflow toe started to collapse in a series of rotational failures. The locations of these failures are marked by the three prominent scarps described above (Fig. 1A), which have cumulatively transported material 50 m in the downslope direction (Fig. 6B). Field observations from March 2017 indicate that these extensional failures are still active: We saw up to 70 cm of vertical offset on individual scarps and 3 m of horizontal displacement at the earthflow–stream channel interface.

1.5.2 Surface Moisture Balance

During the period from 1930 to 2017, mean annual precipitation was 527.3 mm (Fig. 8A), but annual totals vary substantially from year to year and reflect several exceptional climatic events. For example, water year (WY) 1983 delivered an unprecedented 1155.6 mm of precipitation during the strongest El Niño event on record (Wolter and Timlin, 1998). In contrast, WY 2014 brought only 254.0 mm, a

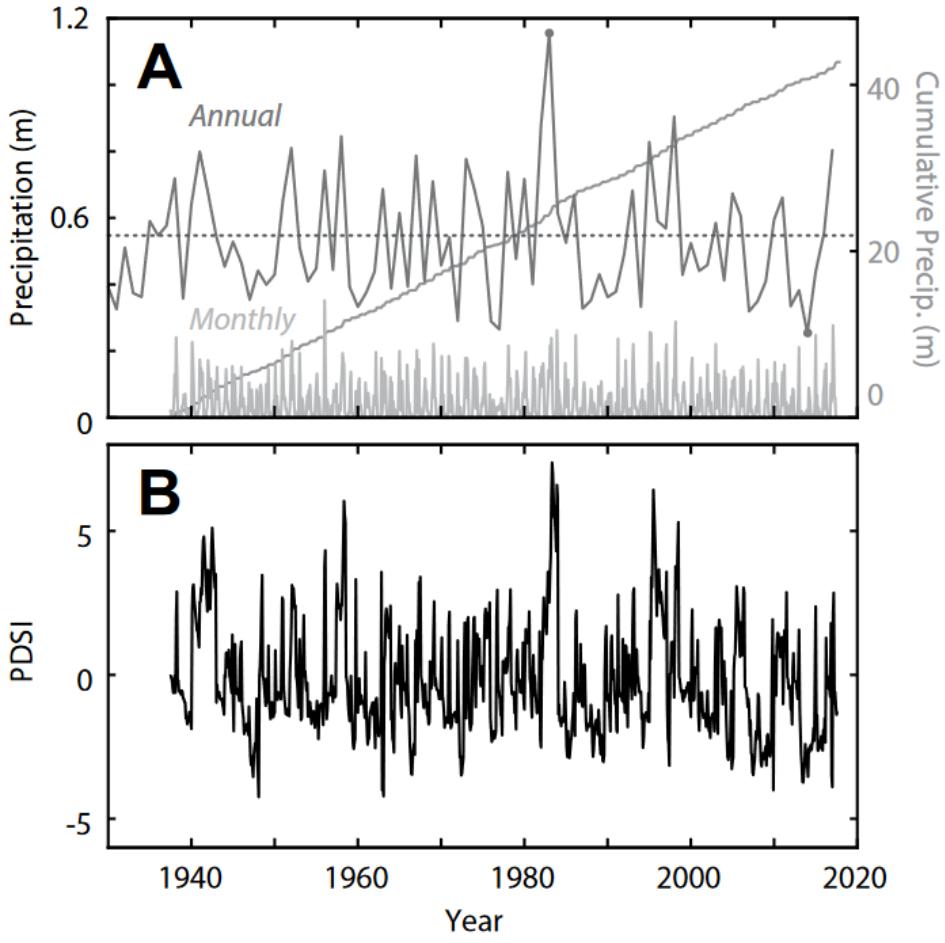

Figure 1.8. (A) Annual (by water year), monthly, and cumulative monthly precipitation, from PRISM Climate Group (2017). Dashed line indicates mean water year precipitation (527.3 mm) for 1930–2017. Gray dots indicate maximum (1156 mm, 1983) and minimum (254 mm, 2014) water year precipitation. (B) Palmer Drought Severity Index (PDSI) calculated using PRISM climate parameters for Oak Ridge earthflow and the code of Jacobi et al. (2013).

record low at the end of an historic, multiyear drought, and is estimated to be the single most arid year in at least the past 1200 yr (Griffin and Anchukaitis, 2014). Even if earthflow velocity is only loosely coupled to precipitation-driven changes in surface moisture balance, the magnitude of the departure of these events from the mean climate state suggests their signal ought to be reflected in the velocity record. While changes in the surface moisture balance do not directly instigate deep-seated slope failure, we note that they can be explicitly linked to changes in basal pore-fluid pressure, which do trigger landslide motion (e.g., Vallet et al., 2015).

Results of the local PDSI calculation are shown in Figure 8B. PDSI values range from about –4 (dry) to +7 (wet), where values <–3 indicate severe or extreme drought. The 1997–1998 El Niño event stands out as the wettest single period on record; however, the period from 1995 to 1999 is also notable for being a prolonged period of wetter-than-average conditions. The average PDSI since 2000 was –0.71, while the average PDSI for the prior 63 yr was 0.04, indicating drier than average conditions since the turn of the century, an observation similar to that of Bennett et al. (2016b).

1.5.3 Velocity Modeling

We determined the power-law exponents that resulted in the best-fit velocity model for each kinematic zone of Oak Ridge earthflow. These exponents are listed in Table 1, along with the RMSE and the probability of observing an RMSE that low (or lower) with a velocity record composed of random values. We calculated probability

by generating 1000 velocity records composed of values drawn at random from an exponential distribution that has the same form as the distribution of our velocity measurements for the kinematic zone in question. We then calculated the RMSE of each random velocity model relative to the measured velocity record to generate a distribution of possible values for RMSE.

Our velocity model yielded significant p-values ($p < 0.05$) only in the UTZ and LTZ, indicating that the PDSI-modeled velocity more closely matches measured velocity in these zones than the records drawn at random. The best-fitting exponent relating PDSI to velocity within the UTZ and LTZ is 4.6, indicating a strongly nonlinear relationship between moisture balance and motion. Indeed, >90% of

TABLE 1. RESULTS OF PDSI-VELOCITY MODELING

Kinematic zone	Best exponent	RMSE	*P* value
Source	10	0.526	0.782
Upper transport	4.6	0.304	0.021
Lower transport	4.6	0.251	0.003
Transition	10	0.387	0.998
Toe	4.9	0.315	0.241

Note: PDSI—Palmer Drought Severity Index; RMSE—root mean square error.

modeled displacement occurs in months that cumulatively make up only 22% of the entire record. Figures 9A and 9B compare the measured and modeled records of normalized velocity and normalized cumulative displacement for the LTZ. We omit plots of velocity and cumulative displacement for the UTZ because after normalization, the trends in velocity between the UTZ and LTZ look very similar.

The fact that the PDSI failed to capture motion for the other kinematic zones is an indication that other drivers of motion may be important in those areas. We discuss possible reasons for the failure of the PDSI-based velocity model in those zones below.

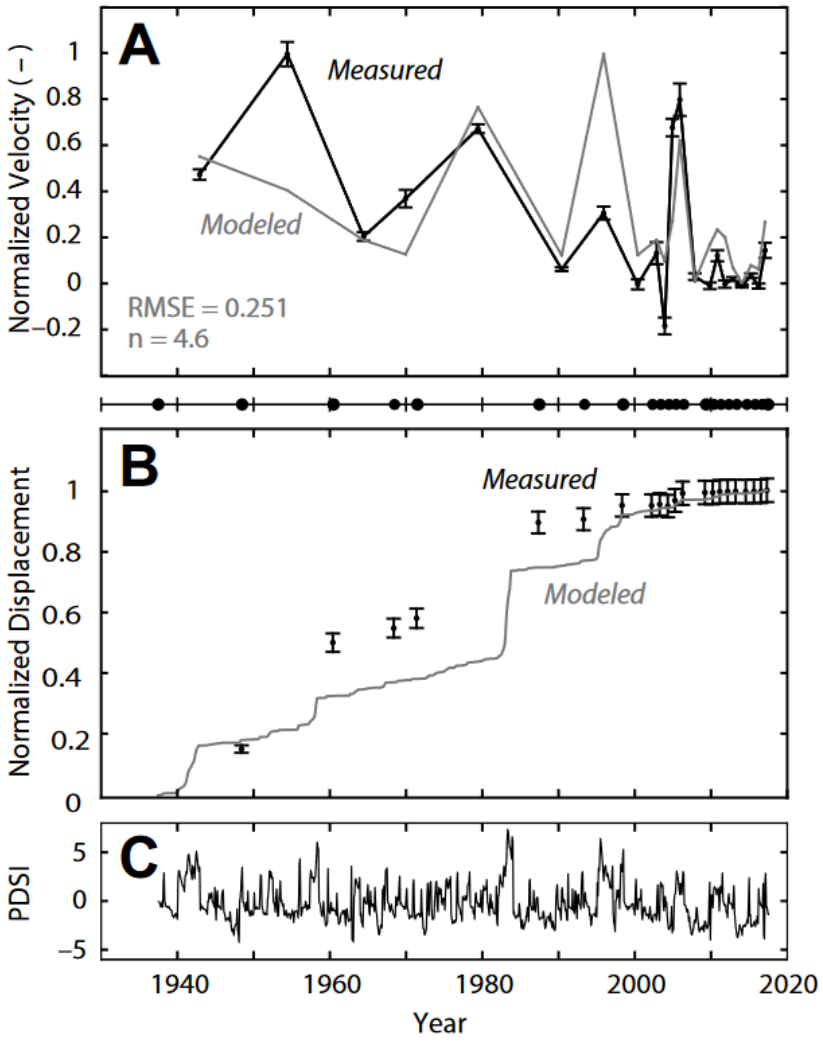

Figure 1.9. (A) Normalized average velocity (measured and modeled) of the lower transport zone (LTZ). Measured values (black) are shown with standard errors. Modeled velocity values (gray) were calculated as a power-law function of the Palmer Drought Severity Index (PDSI), using the best-fit exponent, n = 4.6. (B) Normalized cumulative displacement (measured and modeled) of the LTZ. Modeled results (gray) show monthly values calculated with the bestfit exponent from part A. Black dots along center number line indicate aerial imagery acquisition dates. (C) Palmer Drought Severity Index (PDSI) calculated using PRISM climate parameters for Oak Ridge earthflow and the code of Jacobi et al. (2013), same as Figure 8B. RMSE—root mean square error.

1.6 Discussion

1.6.1 Causes of Nonuniform Landslide Velocity

Our data reveal three primary observations with respect to the spatial variability of movement of Oak Ridge earthflow: (1) The landslide is segmented into distinct kinematic zones that move somewhat independently of one another (Fig. 1A), (2) the velocity of the transport zone increases from north to south (Fig. 3C), and (3) displacement of the transport zone occurs predominantly along the lateral shear surfaces (~70%), with a relatively small component of internal deformation (~30%; Fig. 7).

The emergence of distinct kinematic zones is commonly observed in earthflows and is often attributed to irregularities in basal topography, which can control landslide velocity through changes in slope (Guerriero et al., 2014) or through redistribution of basal pore pressure (e.g., Baum and Johnson, 1993). While we do not have direct observations of the depth, orientation, or roughness of the basal slip surface of Oak Ridge earthflow, we infer that, to first order, its geometry is similar to that of the surface slope. In the case that a landslide has moved a greater distance than the dimensions of its largest basal-topographic irregularities, Coe et al. (2009) has suggested that landslide surface morphology should mimic basal morphology. We think it is very likely that this is the case for sediment in the transport zone of Oak Ridge earthflow over the course of its evolution, given that some areas of the transport zone have moved nearly 300 m in the past 80 yr alone. We also note that the convexity in the long profile of Oak Ridge earthflow is spatially coincident with a

conspicuous break in slope on adjacent, stable hillsides (Figs. 10A–10B). Following from these observations, we suggest that the earthflow convexity is largely the product of downslope regolith transport over the top of this preexisting break in slope.

It is reasonable to link the increase in earthflow slope to the substantial increase in velocity we see from north-to-south within the transport zone over multiple periods (Fig. 3C). In a simple infinite slope approximation (e.g., Lambe and Whitman, 1969), an increase in slope of a critically stable block will result in an excess shear stress acting along the failure plane. This excess shear stress should cause the block to accelerate in accordance with Newton's second law of motion, and, all else being equal, parts of the landslide located on steeper sections of hillslope would be expected to move faster during any given period. Figure 10C shows that the increase in velocity is approximately linear, with an increase in slope for both periods (1937–1948 and 1998–2009), and Figure 3C shows that the increase in velocity appears to start in the same position (distance = 0.5 km) along the profile in both periods despite an elapsed time interval of ~50 yr.

The fact that the spatial break in landslide velocity is not migrating upslope or downslope over time suggests that the clear patterns of landslide velocity that we document do not result from transient kinematic waves that are migrating up or down the landslide in response to either base-level or sediment supply forcing. Iverson (1986b) noted that such kinematic waves should migrate at rates many times faster than the overall landslide velocity. Given that >270 m of landslide motion occurred in the LTZ between 1937 and 2009 (the dates spanned in Fig. 3C), we would anticipate

a clear change in the position of the break in landslide velocity, which is not observed. Consequently, we argue that the gradient of the basal slip surface is the primary governing feature in the observed spatial pattern in landslide velocity.

The historic displacement of a derelict barbed wire fence revealed that ~70% of cross-slope earthflow deformation is concentrated near the lateral shear boundaries of the landslide (Fig. 7). Partitioning of displacement between rigid block sliding and distributed internal deformation is typical of earthflows (e.g., Keefer and Johnson, 1983; Vulliet and Hutter, 1988; Zhang et al., 1991; Simoni et al., 2013) and is key to the physical interpretation of remotely sensed landslide velocities (Booth and Roering, 2011). Because it integrates many years of accumulated motion, the deformation profile we measured from the Oak Ridge earthflow could be productively used as a parameter in future studies of sediment flux or landscape evolution due to earthflows in this region.

1.6.2 Causes of Unsteady Landslide Velocity

In addition to the spatial patterns of velocity that we document above, landslide velocity within each of the kinematic zones of Oak Ridge earthflow is also quite variable over time (Fig. 6). The most-striking aspects of Oak Ridge earthflow's displacement history are (1) large variations in average transport zone velocity over time and (2) apparent slowdown in the transport zone velocity during the past 30 yr. Because the transport zone is also where the bulk of earthflow movement occurred during our 80 yr record, we consequently place particular emphasis on whether

climate, base-level, and/or sediment supply forcing can help us explain these two observations.

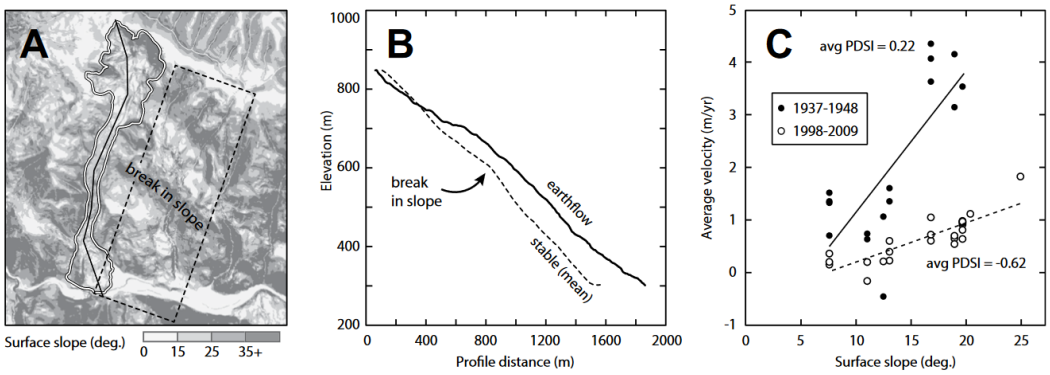

Figure 1.10. Map of topographic slope near Oak Ridge earthflow. Solid white line indicates boundary of earthflow, solid black line indicates location of the earthflow elevation transect in part B, and the dashed black box indicates the sampling zone used to construct the swath profile in part B. (B) Longitudinal elevation transects of Oak Ridge earthflow (solid) and adjacent stable slopes (dashed). The latter depicts a swath profile of mean elevations sampled from inside the dashed black box in part A. Note the spatial coincidence between the earthflow convexity and the break in slope in stable topography. (C) 1937–1948 and 1998–2009 velocity of ground control points (GCPs) in the transport zone vs. surface slope. Velocity increases approximately linearly with surface slope during both time intervals, but the rate of increase was larger during 1937–1948, which was characterized by wetter conditions. PDSI—Palmer Drought Severity Index.

1.6.2.1 Hillslope Debuttressing

We first consider fluvial incision and hillslope debuttressing as a driver of earthflow motion. The observation that earthflows tend to form in relatively steep river canyons in the northern Diablo Range (e.g., Dibblee and Minch, 2005; Wiegers, 2011) supports the notion that hillslope steepening by rivers is an important driver of earthflow motion at some time scale. Indeed, McKean (1993) argued in favor of earthflow response to fluvial incision at historical time scales for a site ~60 km to the north. While we do not have a quantitative record of incision for Arroyo Hondo, it is not necessary in this case because displacement data show a clear lack of connectivity

between the active transport zone and the stream channel. Hence, any effects of debuttressing have so far been buffered by the stability of the "transition" zone (Figs. 5 and 6). All of the observed velocity variations in the transport zone are therefore independent of base level over the time scale examined and must either originate from sediment supply, climate variability, or some combination thereof.

That said, while fluvial debuttressing has not affected the transport zone over this time period, there is evidence it has influenced the toe, which comprises ~20% of the total length of the Oak Ridge earthflow complex and spans nearly the entire floor of the Arroyo Hondo canyon. The toe was largely stationary before the 1990s, until it moved ~25 m between 1993 and 1998, likely in response to precipitation and flooding during the exceptional El Niño event of 1997–1998. The 1998 image shows that floods from this period caused Arroyo Hondo to migrate laterally and erode ~15 m into the hillslope just upstream from the earthflow. Rapid response of the toe was also observed during the above-average precipitation and winter floods of 2017. We measured 3 m of horizontal displacement through the earthflow-channel interface, but no appreciable change in the position of the interface itself. This suggests that Arroyo Hondo was effective at removing earthflow material about as fast as it was delivered to the channel, thus preventing a buttress from strengthening.

We argue that these events, i.e., long-lived buttressing of the toe against the canyon floor and walls, followed by periods of brief, but sometimes intense, fluvial incision in the 1990s, account for the failure of our PDSI-velocity model to capture motion in the toe region (Table 1). That is, velocity seems to be driven by base-level

rather than climate forcing. It is possible that the gravitational collapse of the toe since 1993 may mark the onset of a kinematic wave that will eventually propagate upslope and create a more direct coupling between the transport zone and the stream channel. However, over our 80 yr study period at Oak Ridge earthflow, river incision has not been a meaningful driver of transport zone motion (i.e., the bulk of motion).

1.6.2.2 Availability of Mobile Regolith

We next consider the conceptual model of Mackey and Roering (2011), which appeals to the availability of mobile regolith in an earthflow's source area as a driver for motion. This model is appealing because it provides a ready explanation for the observed long-term slowdown of the transport zone over the past 30 yr (Fig. 6A). As mentioned above, the source area was largely inactive over the entire study period, and the only active alcove fell dormant after 1987, likely due to lack of mobile regolith. Indeed, several of the source zone alcoves consist of steep (>45°) walls from which mobile regolith has been evacuated, exposing relatively fresh sandstone and mudstone bedrock. The lack of sediment supply also appears to be evident in the morphology of the transport zone, where stationary lateral ridges stand high (up to 10 m) above the active earthflow surface in UTZ, but become less well developed in the downslope direction (Fig. 1A). If the tops of these ridges are interpreted as former heights of the active earthflow surface, and there has been no substantial erosion of the basal surface of the earthflow since they were emplaced, as other workers have suggested for similar landslides (e.g., Parise et al.,1997), the modern, active earthflow

is narrower and thinner in the UTZ than it was in the past. Decreasing earthflow cross-sectional area and velocity over our period of observation imply a negative mass balance in this zone, whereas the lack of clear lateral ridges bounding the LTZ implies that the earthflow mass balance is positive there. If there were ridges in this section from a previous episode of earthflow activity, they have been overridden by material in the advancing LTZ lobe.

All other factors remaining constant, we would expect the dormancy of the source zone to induce a decrease in transport zone velocity over time. This is due to the fact that as material is transported downslope without being resupplied from upslope, the landslide should thin, resulting in lower driving stresses. However, to first order, our measurements are inconsistent with this expectation. Instead, they show high decadal variability in transport zone velocity during periods with little-to-no coherent motion in the source zone (Fig. 6). This near-absence of movement in the source zone is likely the primary reason that the PDSI-velocity model performed poorly there (Table 1). Additionally, while decadal velocities in the transport zone decreased after 1987, an acceleration event occurred from 2005 to 2006, during which we measured the highest individual GCP velocity (>10 m/yr) of any image interval in the rec-ord. Last, the supply of mobile regolith seems to have had little influence over the toe region, which was mechanically decoupled from the source and transport zones over the study period and reactivated by fluvial debuttressing after the source zone fell dormant, as discussed above.

For these reasons, we argue that a lack of sediment supply cannot be invoked as the primary driver of temporal velocity variations at Oak Ridge earthflow during our study period, and that the bulk of unsteady movement is tied to a forcing mechanism other than sediment supply from the source zone. At some longer time scale, we recognize that sediment supply must still be critical to the periodicity of earthflow movement: Without any mobile material, the earthflow would cease to exist. At the 80 yr time scale, however, our data do not support its role as the dominant driver of earthflow motion.

1.6.2.3 Changes in Surface Moisture Balance

Given the large variability in surface moisture balance over time, we suspect that this driver is the most plausible explanation for unsteady motion in the transport zone. In support of this view, we note that our PDSI-driven velocity model does well at representing displacement within the transport zone in many respects. First, the best-fitting exponent relating PDSI to velocity within the UTZ and LTZ is 4.6, which is consistent with the idea that landslide velocity is a strongly nonlinear function of pore-fluid pressure, as would be expected for a Coulomb failure process. Second, it creates a history of movement with episodic "surges" separated by longer periods of slow movement (Fig. 9B). Again, >90% of modeled LTZ displacement occurred in months that cumulatively account for only 22% of the entire record. We note that the pattern of steady motion or quiescence punctuated by episodic accelerations is commonly observed for earthflows (Hungr et al., 2014), suggesting our simplified

approach is capturing some aspects of the rich dynamics associated with these landslides.

In particular, the model does a good job of capturing low average velocities in 1960–1971, 1987–1993, 2000–2004, and 2006–2017. In addition, the model captures the surges that occurred during the winters of 1983 and 2005–2006. In contrast, the model struggles with the amount of movement in other intervals: It underpredicts velocity in 1948–1961 and overpredicts it in 1993–1998. Figure 9B emphasizes the preceding points by showing cumulative monthly displacement, as integrated from the best-fit PDSI velocity model for the LTZ.

We hypothesize that the disagreements between our measured and modeled velocity records may be related, in part, to the decrease in sediment supplied to the transport zone over the study period, since a decrease would serve to restrain velocities during wet periods near the end of our record, such as 1993–1998, where our model overpredicted displacement (Figs. 9B–9C). Furthermore, we propose that we can consider the superimposed effects of moisture balance and sediment supply on the unsteady velocity of the transport zone by weighting the PDSI term in our velocity model as follows:

$$Vmodeled = (Ss \times PDSI)^n, \quad (2)$$

where *Ss* is a sediment supply term between zero and one. Since the source zone of the earthflow fell dormant after 1987, the value of *Ss* should decrease over time according to some function. We ran models with both exponential and single-step decreases in *Ss* and determined that a step function where *Ss* decreased from 1 to 0.75

in the month of October 1982 and n = 3.8 provided the best agreement between the measured and modeled LTZ velocity records (RMSE = 0.216, p = 0.001; Fig. 11). The inclusion of sediment supply represents an improvement over the PDSI-only

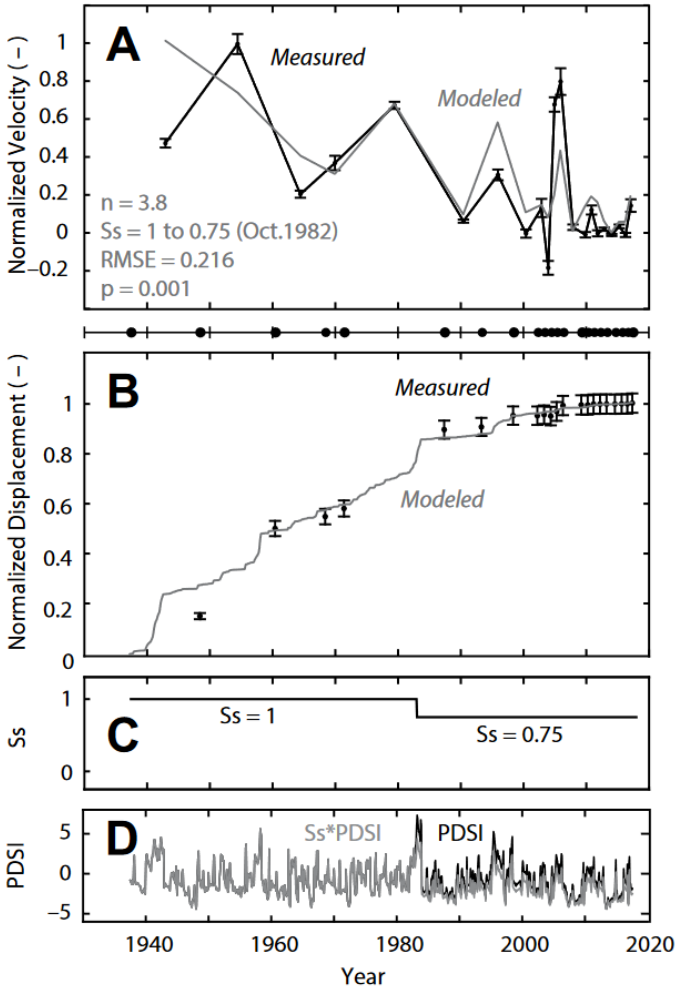

Figure 1.11. (A) Normalized average velocity (measured and modeled) of the lower transport zone (LTZ). Measured values (black) are shown with standard errors. Modeled velocity values (gray) were calculated as a power-law function of PDSI × Ss, using the best-fit exponent n = 3.8 and the best-fit Ss drop from 1 to 0.75 in October 1982, where PDSI is the Palmer Drought Severity Index, and Ss is a sediment supply term between zero and one. RMSE—root mean square error. (B) Normalized cumulative displacement (measured and modeled) for the LTZ. Modeled results (gray) show monthly values calculated with the best-fit parameters in part A. Black dots along center number line indicate aerial imagery acquisition dates. (C) Value of Ss over time for the best-fit model run. The model was allowed to choose the magnitude of the drop in Ss as well as the month to apply the drop in order to maximize agreement with measurements. (D) Monthly values of unadjusted PDSI compared to the value of Ss × PDSI for the best-fit model.

model presented in Figure 9. The fact that the model identified October 1982 as the month in which a step decrease in sediment supply ought to have occurred is consistent with the independent observation of source zone dormancy starting in the 1980s. Also as a result, the model better captures the magnitude of motion from 1993 to 1998 than it did in the PDSI-only version and shows that sediment supply effects start to become important at the multidecadal time scale.

In the transport zone, the temporal variability of earthflow velocity due to surface moisture balance and sediment supply is also superimposed on top of the spatial variability of earthflow velocity due to the topographic slope of the underlying failure plane. This is demonstrated in Figure 10C, in which transport zone velocity is shown to increase with topographic slope in two different time intervals separated by over 60 yr (1937–1948 and 1998–2009). The fact that the rate of increase in velocity is higher in the 1937–1948 interval probably reflects the fact that wetter average conditions prevailed during this period (mean PDSI = 0.22) than the period from 1998 to 2009 (mean PDSI = –0.62).

1.7 Long-term Evolution of Oak Ridge Earthflow

The morphology and kinematic history of Oak Ridge earthflow reveal that all of the aforementioned drivers, namely, the changes in depth, slope, and pore pressure that accompany perturbations in sediment supply, base level, surface moisture balance, and the slope of preexisting topography, are necessary to provide a satisfying explanation for its movement over the past 80 yr. Specifically, the conceptual picture

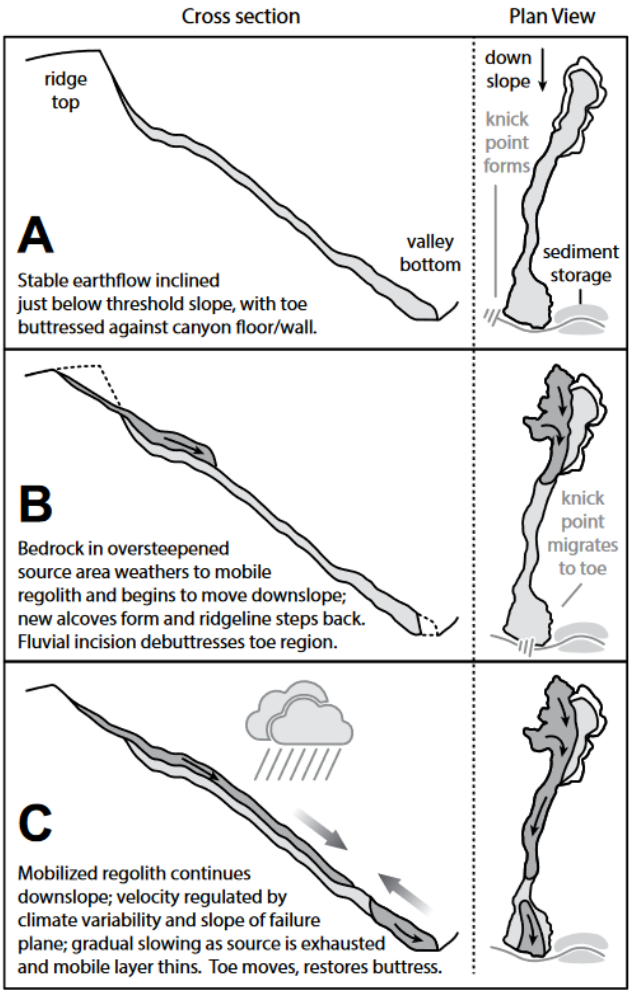

Figure 1.12. Conceptual model for the evolution of Oak Ridge earthflow. Stages are described in the panels and text.

that emerges from our data is one in which spatial patterns of earthflow velocity within the transport zone are governed largely by the slope of the underlying failure plane, whereas temporal patterns are governed largely by climate-driven changes in surface moisture balance, with a secondary role for sediment supply. Evidence for transient waves of motion in response to fluvial debuttressing is limited to the toe, with no observed connections to the greater earthflow. This is consistent with the

results of Iverson (1986b), which showed that even for landslides with a wide range of material properties, significant, multiyear sediment flux perturbations at the toes may never migrate to the headscarps.

Figure 12 depicts our conceptual model in a time series of schematic cross-sectional and plan-view drawings. Since we do not have data to constrain the origin or initial failure of Oak Ridge earthflow, we begin with a preexisting earthflow that extends from ridge top to valley bottom (Fig. 12A) and has an undulating surface topography that largely reflects the geometry of the underlying failure plane. Near the ridgeline, fresh bedrock is exposed along the headscarp. In the valley bottom, the earthflow toe forms a buttress against the canyon floor and walls, which lends stability to the slide. In response to earthflow encroachment into the stream channel, a fluvial knickpoint exists on the downstream end of the toe, while fluvial sediment is impounded at the upstream end. Over time, as fresh bedrock in the source zone weathers to mobile regolith, it is transported from the steep headscarp walls into the transport zone by various mass-wasting processes (Fig. 12B). This creates new, bowl-shaped alcoves and results in a back-stepping of the ridgeline.

As time passes, regolith from these alcoves continues to move downslope, overriding older earthflow deposits as it advances (Fig. 12C). The spatial variability in velocity of this mass is controlled by the topographic slope of the basal failure plane, and the temporal variability in velocity is controlled by climate-driven changes in basal pore pressures. As the supply of mobile regolith in the source zone is exhausted, the upper earthflow thins and slows down, and velocity becomes less

sensitive to climate variability overall. Meanwhile, in the stream channel, the knickpoint propagates upstream until a substantial portion of the toe becomes debuttressed. This initiates a new sediment flux perturbation at the base of the earthflow that propagates upslope.

This conceptual model is consistent with existing models of long-term earthflow evolution, such as that of Mackey and Roering (2011), who described the supply of mobile regolith in the source zone as the ultimate control on the periodicity of earthflow movement. However, in the case of Oak Ridge earthflow, the time scale of our observations may be too short to fully see the supply effects manifested. The fact that moisture balance (PDSI) appears to be the dominant factor influencing the temporal variability in velocity suggests that the lag time between stabilization of the source zone and potential stabilization of the transport zone is longer than our 80 yr observation period.

Figure 12C represents the present-day configuration of Oak Ridge earthflow, consistent with our observations to date. We note that two major sediment flux perturbations seem to be present, one with origins in the source zone and one with origins at the toe, which are migrating in opposite directions. In principle, it should be possible to more precisely estimate the time scales and distances over which these perturbations will migrate in the future, using a kinematic model for landslide response like that of Iverson (1986a, 1986b). We currently lack many of the constraints (e.g., spatial/temporal variability of landslide depth, slope, and water table elevation) to confidently apply such a model here; however, we anticipate that

continued data collection at this site will enable us to make these estimates in the future.

1.8 Conclusions

Prediction and mitigation of the effects of slow landslides require not just an analytical framework that can incorporate the diverse drivers of landslide motion, but also historical data that can be used to assess nonuniform, unsteady landslide motion in light of these drivers. Toward this end, we assembled an 80 yr (1937–2017) record of movement for Oak Ridge earthflow in California's northern Diablo Range. We used this kinematic history, observational evidence, and a PDSI-based kinematic model to consider several possible drivers of unsteady, nonuniform earthflow movement, including: variations in slope of the basal failure plane, a lack of mobile regolith supply from the source, fluvial debuttressing from below, and changes in climate forcing over time. All of these aforementioned drivers appear necessary to provide a satisfying explanation for movement at Oak Ridge earthflow. In particular, spatial patterns of earthflow velocity within the transport zone are governed largely by the slope of the underlying failure plane, whereas temporal patterns are governed largely by climate-driven changes in surface moisture balance at the annual-decadal scale, as indicated by our PDSI-based velocity models. Declines in sediment supply acted as a secondary control on temporal velocity variations over our study period; however, the influence of this driver likely grows at longer time scales. Evidence for transient waves of motion in response to fluvial debuttressing is limited to the toe,

and continued monitoring of Oak Ridge earthflow is required to determine whether those perturbations in sediment flux will migrate further upslope. We consider simple kinematic models based on surface moisture balance, like the one developed here, to be useful tools in the evaluation of the relative roles of multiple drivers of earthflow motion over many decades. Benefits of this type of analysis are that it requires only repeat aerial imagery and time-series values of temperature and precipitation. It can be easily modified with sediment supply and hillslope debuttressing parameters to either amplify or dampen the effects of climate variability over time and may prove useful for predicting earthflow activity in the future.

1.9 Acknowledgements

This material is based upon work supported by a National Science Foundation (NSF) Graduate Research Fellowship awarded to A. Nereson and an NSF grant (Geomorphology and Land-Use Dynamics, EAR-1658800) to N. Finnegan. Further support came from the Casey Moore Fund and from the Northern California Geological Society's Richard Chambers Memorial Scholarship in awards to A. Nereson. We are grateful to Joshua Roering and Meng-Long Hsieh for constructive reviews of this manuscript and thank the San Francisco Public Utilities Commission and Russ Fields for site access.

Chapter 2.

Field and Remote-Sensing Evidence for Hydro-mechanical Isolation of a Long-Lived Earthflow in Central California

Previously published as:

Nereson, A.L., Davila Olivera, S., Finnegan, N.J. (2018) Field and remote-sensing evidence for hydro-mechanical isolation of a long-lived earthflow in central California, Geophysical Research Letters, 45, 9672-9680, https://doi.org/10.1029/2018GL079430

2.1 Abstract

Persistent motion of slow-moving landslides has been linked to entrapment of water in slide masses by weak, low-permeability shear zones at their basal and lateral margins. This so-called "bathtub effect" should have remotely sensible effects on soil moisture and vegetation health. Here we assess this effect at a seasonally active earthflow in northern California with analysis of soil properties and nine years (2009-2018) of multispectral satellite imagery. The shear zone has low hydraulic conductivity, and the earthflow shows elevated water content relative to its surroundings. Spectral indices suggest that the earthflow is perennially wetter, and its

vegetation thrives for longer into the dry season as a result. The magnitude of the bathtub effect is correlated with cumulative multiyear rainfall, and its surface expression disappears during the driest year of the 2012-2015 drought. These findings demonstrate a new method for identifying and monitoring mechanical and hydrological interactions that enable persistent landslide motion.

2.2 Plain Language Summary

The ability of some landslides to move slowly and persistently for many years without accelerating catastrophically may be linked to entrapment of rain water in slide masses by slow-draining boundaries at their sides and bottoms. The existence of this so-called “bathtub effect” can be tested for directly with soil analysis but should also have visible effects on soil moisture and vegetation health that can be measured remotely using satellite imagery. We examined a seasonally active landslide in northern California with slow-draining boundaries and elevated water content relative to its surroundings. Nine years (2009–2018) of satellite imagery suggest that the earthflow is perennially wetter and its vegetation thrives for longer into the dry season as a result. The magnitude of this effect is correlated with cumulative multiyear rainfall. These findings demonstrate a new method for identifying and monitoring the hydrology and movement of persistent landslides.

2.3 Introduction

Persistent movement of deep-seated (>5 m), slow-moving (<10 m/a) landslides is a common phenomenon with important scientific and practical implications. These landslides, often referred to as earthflows (Hungr et al., 2014), can dominate erosion in mountainous landscapes (Bennett, Miller, et al., 2016; Mackey & Roering, 2011), control the long-term evolution of catchment geometry (Booth et al., 2013), and cause progressive damage to infrastructure and property over time (Bertolini et al., 2005).

At relatively short timescales, earthflow movement is regulated by precipitation-driven changes in pore water pressure at the basal shear surface (Baum et al., 2003; Iverson, 2000, 2005). Annual cycles of movement in response to seasonal rainfall are commonly reported (Handwerger et al., 2013; Hilley et al., 2004; Iverson & Major, 1987; Keefer & Johnson, 1983; Kelsey, 1978); however, earthflows also experience longer-term slow-downs during multiyear droughts (Bennett, Roering, et al., 2016), and some show sensitivity to small, short-lived pressure perturbations from individual thunderstorms (Coe et al., 2003) or atmospheric tides (Schulz et al., 2009). Historical observations demonstrate that earthflows with this type of recurring motion can persist for decades or centuries (e.g., Bovis, 1985; Crandell & Varnes, 1961; Del Soldato et al., 2018; Mackey et al., 2009; Roering et al., 2015), while geologic and geochronologic evidence further suggests that some may be active for millennia (Bennett, Miller, et al., 2016; Bovis & Jones, 1992; Madole, 1996; McSaveney & Griffiths, 1987).

Slow, persistent earthflow motion requires complementary mechanisms to repeatedly reactivate previously failed materials and to limit velocity during periods of activity. Baum and Reid (2000) linked persistent reactivation of large translational landslides to entrapment of water in landslide masses by weak, low-hydraulic conductivity clay layers in basal and lateral shear zones. These fine-grained layers, which may form by physical breakdown of larger grains or by migration of coarser grains away from the shear zone (Skempton & Petley, 1967), tend to isolate a landslide both mechanically and hydrologically from adjacent, unfailed materials. This effectively destabilizes the slide by weakening its shear zone and allowing it to fill with water like a bathtub. The soil characteristics and behavior of many earthflows are consistent with the bathtub effect, suggesting its widespread influence in nature (Allen, 2016; Baum & Fleming, 1991; Baum & Reid, 2000; Coe et al., 2003; Handwerger et al., 2013; Savage & Wasowski, 2006).

Once stresses evolve to make an earthflow unstable, its velocity must be regulated by another mechanism. Commonly invoked mechanisms typically involve pore pressure feedback related to slip-surface roughness (Baum & Johnson, 1993) or dilation of dense, fine-grained shear zone soils (Iverson, 2005). The bathtub effect may be complementary to these mechanisms. The former accounts for the presence of dense, dilation-prone soils at the base of landslides and provides a mechanism for pore pressures to repeatedly rise to (or, perennially maintain) critical values, while the latter accounts for slow, non-catastrophic failure.

The bathtub effect entails a profound difference in the hydrology of earthflows, including shallow water table depths (e.g., Iverson & Major, 1987) relative to adjacent, stable slopes. In loamy soils characteristic of earthflow-prone landscapes (e.g., Brown & Ritter, 1971), capillary rise may dampen soil several meters above the water table (Fetter, 2001), thereby increasing soil water available for plant transpiration, particularly during meteorologically dry conditions. We hypothesize that the resulting differences in soil moisture and its influence on vegetation health can be captured in high-resolution, remotely sensed, multispectral imagery. We tested this hypothesis at Oak Ridge earthflow, a long-lived, seasonally active landslide in California's northern Diablo Range. We sampled and analyzed earthflow soils for grain size, moisture content, Atterberg limits, residual friction angle, and saturated hydraulic conductivity to confirm the presence of bathtub-like conditions. We then used a nine-year time series of 97 multispectral RapidEye images to track changes in the reflectance characteristics of Oak Ridge earthflow as proxies for soil moisture and vegetation health.

2.4 Study Site

Oak Ridge earthflow is a seasonally active landslide in the northern Diablo Range, 20 km northeast of San Jose, California (Figure 1a). It is 1.8 km long (area = 0.35 km^2), has 600 m of relief, and has an average slope of 17°. In its fastest section (the transport zone), Oak Ridge earthflow moved >275 m between 1937 and 2017. Average velocity was linked to variability in surface moisture balance and upslope

sediment supply (Nereson & Finnegan, 2018). Local bedrock consists of the Mesozoic-early Cenozoic Franciscan Complex (Rubin, 2002). Franciscan lithologies are dominated by metamorphic sandstones and mudstone mélanges and are highly susceptible to hillslope failure and earthflow processes (Handwerger et al., 2013; Keefer & Johnson, 1983; Kelsey, 1978; Mackey & Roering, 2011; Scheingross et al., 2013).

Oak Ridge earthflow is subject to a Mediterranean climate, with hot, dry summers and mild, wet winters. Average annual precipitation is 52.7 cm (20.7 in) and falls mainly as rain between the months of October and April (PRISM, 2017). Vegetation is primarily nonnative annual grassland, with some oak savanna, mixed evergreen woodland, and minor amounts of Diablan sage scrub (SFPD, 2008). Plant production in these annual grasslands occurs in winter and spring.

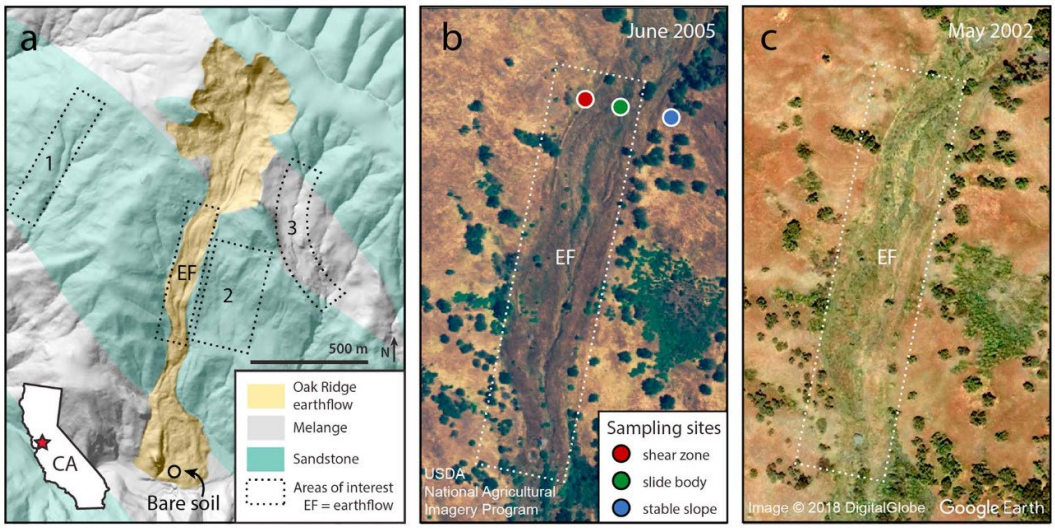

Figure 2.1. (a) Hillshade map of Oak Ridge earthflow. Bedrock units after Dibblee and Minch (2006) and Graymer et al. (2006). (b and c) Natural-color images of earthflow AOI (zoomed extent from (a)).

Oak Ridge earthflow is well suited for this study because of the relatively consistent grassland vegetation type across the study area and the highly seasonally rainfall pattern, which entails that vegetation must rely on preexisting soil moisture reserves for months at a time. Moreover, some aerial images of the site show a striking visual contrast between the earthflow and its surroundings (Figures 1b and 1c), suggesting surface manifestations of the potential bathtub effect will be large enough to measure.

2.5 Methods

2.5.1 Soil Sampling and Analysis

In October 2016, we used a hand auger to collect soil samples to depths of 1 m below the ground surface(bgs) from the lateral shear zone, the earthflow body, and the stable hillslope immediately adjacent to the earthflow (Figure 1b). We processed soil samples to determine their water contents, bulk densities, grain size distributions, and Atterberg limits (Text SI). Atterberg limits correlate with hydraulic conductivity and shear strength, so we evaluated our results with respect to existing empirical relationships. The residual friction angle of one shear zone sample was measured using a multistage ring-shear test (Text S1)[1]. We also used the Kozeny-Carman equation (Chapuis, 2012) to calculate saturated hydraulic conductivity (K [m/s])

[1] Supporting information can be found online at https://agupubs.onlinelibrary.wiley.com/doi/full/10.1029/2018GL079430

based on the liquid limit, specific gravity, and void ratio of individual samples (Chapuis & Aubertin, 2003, Text S1).

2.5.2 Remote Sensing of Soil and Vegetation

We analyzed 97 multispectral images captured by the RapidEye constellation of satellites between 2009 and 2018. RapidEye images have a spatial resolution of 5 m and contain blue, green, red, red-edge, and near-infrared bands. We downloaded all imagery from Planet Labs (2018) at an approximately monthly temporal resolution and converted digital pixel numbers for each band from at-sensor radiance to reflectance (Text S2). We extracted reflectance values from four areas of interest (AOI): one that encompasses the transport zone of Oak Ridge earthflow and three on adjacent, stable slopes (Figure 1a). The stable-slope AOI are of comparable size (~1,500 pixels) to the transport zone and share similar grassland vegetation, topographic slopes, and aspects (Text S2).

We used two metrics to quantify differences in spectral reflectance between the earthflow and adjacent stable slopes: the soil line index (SLI; Wiegand & Richardson, 1982) and the weighted difference vegetation index (WDVI; Clevers, 1988). SLI can be useful as an index of soil moisture (e.g., Gao et al., 2013), while WDVI indicates relative abundance and activity of green vegetation (Jensen, 2007). Both metrics describe the position of pixel values with respect to the "soil line" in red and near-infrared spectral space (Text S2 and Figure S1). McKean et al. (1991) also used pixel

trajectories in this spectral space to characterize differential-velocity zones in slow-moving earthflows.

2.6 Results

2.6.1 Soil Properties

Soils encountered in the shear zone were fine-grained and classified according to ASTM standard D 2487(ASTM, 2008) as sandy lean clay with gravel. The soils from the earthflow body and stable slope were coarse-grained and classified as silty sands with gravel. Grain size distributions for the lowest five samples (between 50 and 100 cm bgs) from all three boreholes are shown in Figure 2. Soils from both earthflow sites have a bimodal grain size distribution with one peak in the silt-clay range and one in the sand range; however, the shear zone contains a relative abundance of grains smaller than fine silt (<10–2 mm). In contrast, the soils from the stable slope have one primary peak in the sand range.

Water content increased with depth in each borehole by 3–8% (Figure 2b). The shear zone had the highest water content in every depth interval and displayed the largest increase in water content with depth (from 6 to 14%). Conversely, soils from the stable slope had the lowest water content at every depth. In the deepest samples (95 cm bgs), the difference in water content between the shear zone and earthflow body was 7%, whereas the difference between the shear zone and the stable slope was

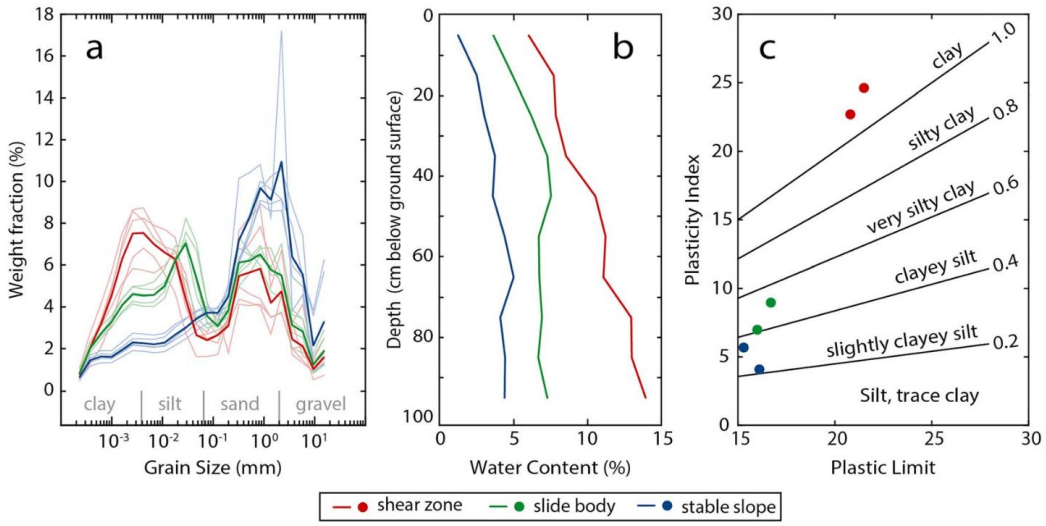

Figure 2.2. Measured soil properties, including (a) grain size distributions (the bold lines indicate average of samples from each site), (b) water content, and (c) Atterberg limits. Liquid limit can be inferred as PL + PI. Contours of Cohesive Index shown in black.

10%. Sampling occurred at the end of the summer dry season; thus, measured water contents should represent minimum annual values.

Atterberg limits are reported in Figure S3 but are summarized in Figure 2c using the cohesive index diagram of Cornforth (2005). Shear zone samples have relatively high liquid limits (LL = 44–46) and plasticity indices (PI = 23–24) relative to samples from the other sites and have cohesive indices much closer to those of clay than silt (cohesive index = 1.1). The residual friction angle of shear zone material determined by ring shear tests (12–14°; Figure S2) was low compared to values determined for other earthflows in California (Keefer & Johnson, 1983; Schulz et al., 2018). Several studies report decreasing peak and residual φ_0 with increasing LL and PI (e.g., Terzaghi et al., 1996, p. 152; Stark & Hussain, 2013; Sorensen & Okkels, 2013). These relationships suggest that φ_0 is lower in the shear zone by as much as ~5–10°, given the ranges of LL and PI measured in adjacent materials.

The Kozeny-Carman equation yielded an average saturated hydraulic conductivity of 2.6 * 10^{-6} m/s for the shear zone, a value typical of sandy silts (Fetter, 2001, p. 85). Saturated hydraulic conductivity of the earthflow body (4.4 * 10^{-4} m/s) and stable slope (8.2 * 10-^{4} m/s) were ~2 orders of magnitude larger than the shear zone, with values typical of well-sorted sands.

2.6.2 Remote Sensing of Soil and Vegetation

Figure 3 shows pixel trajectories of earthflow and stable slope reflectance in red and near-infrared spectral space. Each point represents the average reflectance values of all earthflow (or stable-slope) pixels for a given image. The soil line shown in Figure 3 is the best-fit line to bare soil reflectance measured from a small patch of soil (30 pixels large) exposed by shallow mass wasting near the earthflow toe in March 2017 (Figure 1a).

In general, at the start of a calendar year, pixels from both earthflow and stable-slope AOI had low red and near-infrared reflectance values (~0.1). During the wet-season months of February–April, near-infrared reflectance increased rapidly with respect to red reflectance as grassland vegetation developed, resulting in a departure of pixel values away from the soil line. Maximum perpendicular departures from the soil line occur in April–May before collapsing back toward the soil line by June. In June–July, reflectance plotted close to the soil line, but continued to increase in value. Between July and August, both red and near-infrared reflectance decreased below

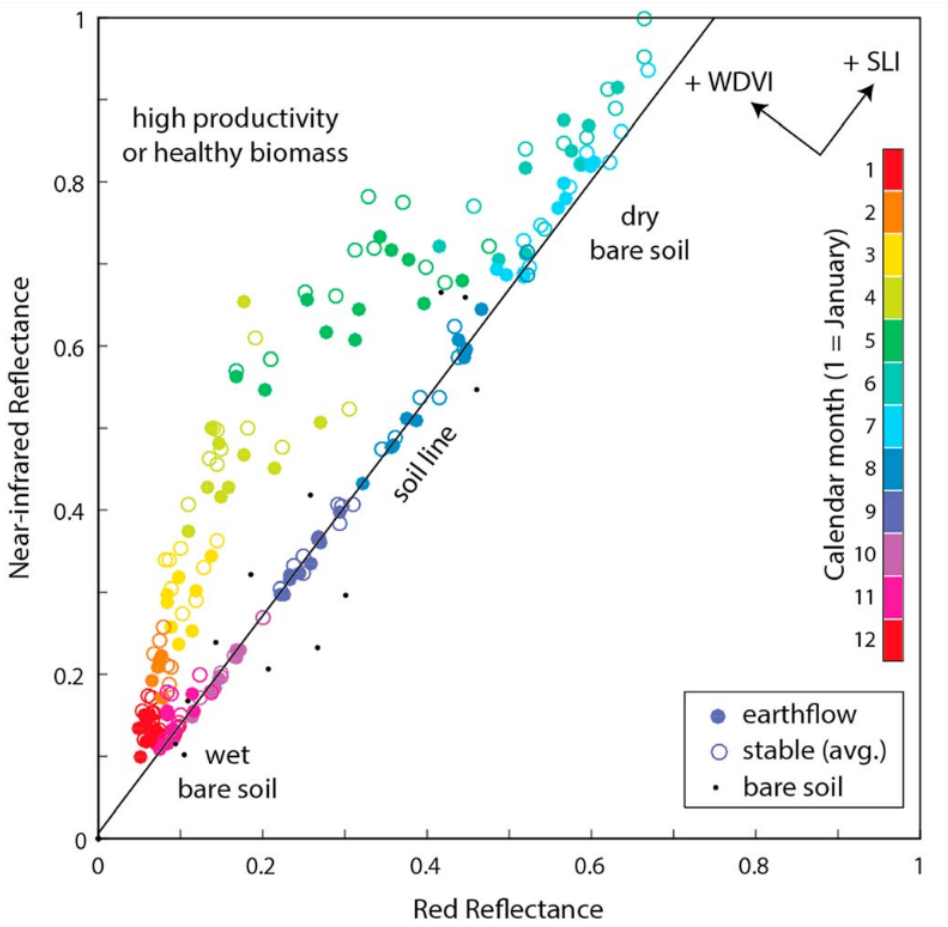

Figure 2.3. Average red and near-infrared reflectance values from earthflow and stable-slope AOI. The filled dots represent mean of all pixels in earthflow AOI for a given image. The unfilled dots represent mean of all pixels on all three stable AOI for a given image.

maximum values, but values still clustered tightly along the soil line. This migration of pixels *d*ownward along the soil line continued through December (Figure 3).

WDVI changed cyclically over the course of a year for both the earthflow and stable slopes (Figure 4a). It gradually increased toward maximum values (~0.3–0.4) in April–May indicating maximum vegetation productivity at that time, before rapidly decreasing to ~zero by July and remaining at low values until January. The pattern of WDVI over time is similar to that of gross primary productivity and ground-based

normalized difference vegetation index reported for an annual grassland 80 miles northeast of Oak Ridge by Liu et al. (2011) and Liu et al. (2017). They showed that at the beginning of the growing season, soil water in the upper 20 cm was sufficient for vegetation needs, but low temperatures and limited photosynthetically active radiation caused grasses to grow slowly. In the spring, warmer temperatures and longer days contributed to the fast grass growth until a peak in March or April, after which soil moisture rapidly declined, along with grass growth. The similarity of WDVI patterns to the productivity data of Liu et al. (2011) suggests that this metric provides a reasonable depiction of grassland growth at Oak Ridge earthflow.

The difference in WDVI (ΔWDVI = stable average minus earthflow) gradually increases every winter-spring (January–May), before abruptly decreasing toward zero in June–July (Figure 4b). Between July and December, when WDVI is low, ΔWDVI typically remains relatively low as well, coincident with periods of low vegetation productivity. In several years, ΔWDVI dropped below zero for one or two months in late spring-early summer, indicating greater vegetation productivity or healthier biomass on the earthflow for this short, but semi-regular interval over time.

SLI varies cyclically over the course of a year (Figure 4c). In January, SLI was typically ~0.1 but gradually approached 1 by June–July. The difference in SLI (ΔSLI = stable average minus earthflow) was positive (i.e., drier stable slopes) for almost every image in the record and maximum values typically occurred in June–July, during the seasonal dry period. In addition to WDVI and SLI, we calculated time

series of other common vegetation indices; however, the patterns in these indices were similar to WDVI, so they are omitted for brevity (Figure S4).

2.7 Discussion

Our results confirm that Oak Ridge earthflow shares key characteristics in common with the persistently active, bathtub-like landslides described by Baum and Reid (2000). Soil tests verify that where measured, the shear zone is made of relatively weak, impermeable, fine-grained soils with respect to adjacent materials. Also, water content measurements demonstrate that the earthflow retained more water relative to the stable slope over the duration of at least one dry season during water year 2016 (Figure 2b). Since it is common for large, deep-seated landslides to exhibit heterogeneous material properties (e.g., Vallet et al., 2015), it is unlikely that measurements are wholly representative of all other points in the landslide. That said, their consistency with the bathtub model is sufficient to justify further analysis of satellite imagery to determine whether a spectral bathtub effect can be identified.

Our analysis of the available multispectral imagery revealed two key observations. First, WDVI is typically higher on stable slopes than on the earthflow, except for short periods in the late spring or summer of some years. Second, the SLI is nearly always higher for stable slopes than for the earthflow. The tendency for stable slopes to be characterized by higher WDVI (Figure 4b), especially during the wet winter months, initially seemed inconsistent with an active bathtub effect at Oak Ridge earthflow. We expected preferential water retention in the landslide to result in

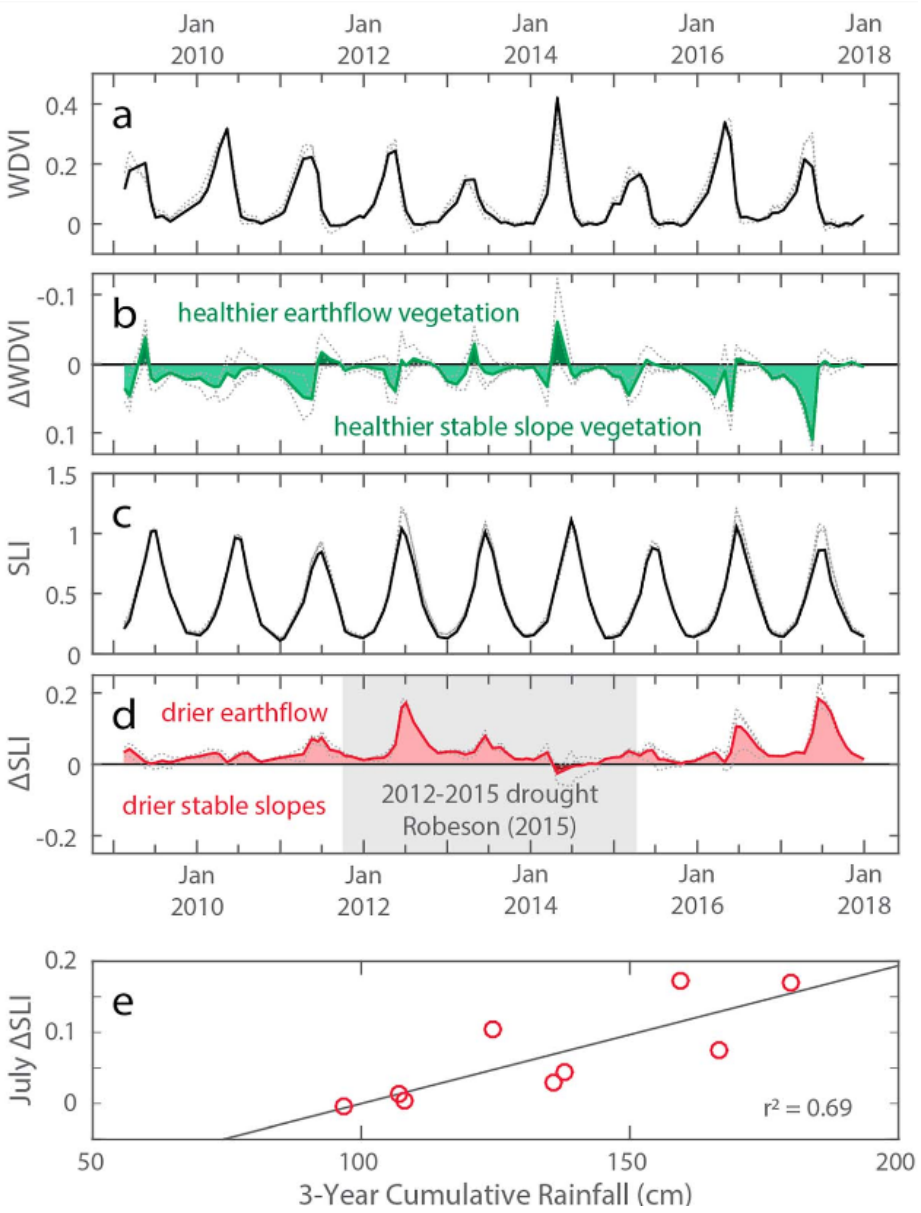

Figure 2.4. (a) WDVI and (c) SLI over time. The bold lines indicate average of all earthflow pixels. The dotted gray lines indicate average of pixels in each stable AOI. (b) ΔWDVI and (d) ΔSLI over time. The bold green and red lines indicate the difference calculated using the average spectral index value from all three stable AOI. The dotted gray lines indicate the difference between each individual stable AOI and earthflow AOI. (e) July ΔSLI versus three-year cumulative water year rainfall.

a year-round positive effect on grassland productivity relative to stable slopes.

However, this apparent inconsistency might be due to the fact that annual grasslands

in California are not typically water limited during the wet, winter months, even on stable slopes (Liu et al., 2011). Hence, extra water content in earthflow soil would have had little positive impact on nascent grasses when other limiting factors, like photosynthetically active radiation and air temperature, were at seasonal lows. Indeed, the excess moisture may actively inhibit productivity of grasses if the soil becomes waterlogged. Saturated conditions reduce root water permeability in many plants, causing them to experience "physiological drought" and a decline in productivity (Shahzad et al., 2016). Our field observations from 2016 and 2017 confirm that water-logged soils and ephemeral ponds were common on the earthflow, but not on adjacent stable slopes, during the winter months (Figure S5).

Despite generally higher values of average WDVI on stable slopes, there were short but regularly spaced periods of time during which the opposite was the case. Although the magnitude of ΔWDVI was typically small during these periods (Figure 4b), the seasonal regularity of this occurrence for approximately one month during the late-spring or summer of most years suggests that it represents an actual difference in grassland phenology between earthflow versus adjacent, stable slopes. We interpret these short periods of negative ΔWDVI as an ecological consequence of the bathtub effect, where the senescence of earthflow grass lags behind that on stable slopes as a result of higher soil water availability in the landslide.

Reflectance data show that ΔSLI is greater than zero in nearly every image for each of the three stable AOIs (Figure 4d). Assuming similar soil reflectance characteristics and vegetation cover fraction between the earthflow and stable-slope

AOI (Text S4), this suggests that earthflow soil moisture was relatively high compared to stable slopes for most of the record, which is consistent with our measurements of elevated water content at the end of a summer dry season. Seasonal peaks in ΔSLI indicate that there were years, and specific times of year, during which the earthflow may have been especially wet relative to adjacent stable slopes. In winter, when moisture would have been relatively abundant in the near-surface of the landscape, ΔSLI was low, but during the summer dry-down, that relative difference grew to maximum annual values by around July of each year, presumably due to the bathtub effect (Figure 4d). The only period in which average ΔSLI dropped below zero was in summer 2014. Notably, water year 2014 came near the end of an historic, multiyear drought with record-low annual precipitation (254 mm) and was the most arid in the 1895–2014 instrumental record (Robeson, 2015). This exceptional climatic event likely dried out the landscape so thoroughly (i.e., drained the bathtub) that any excess water retained within the earthflow body was decoupled from surface moisture conditions (e.g., by insufficient capillary rise).

To more directly consider this relationship between precipitation and magnitude of the bathtub effect over time, we plotted ΔSLI from July of each year as a function of cumulative precipitation from the previous one through five water years (PRISM, 2017). In a year (or years) with higher rainfall, we suspected that the earthflow would retain more water, and thus, ΔSLI should be more pronounced during the summer dry-down. We found a weak positive relationship ($r^2 = 0.22$) between the prior year's annual rainfall and July ΔSLI. The correlation was improved when we included

cumulative rainfall from the previous two water years, was maximized with three water years ($r^2 = 0.69$; Figure 4e), and was diminished for four and five years (Figure S6).

The weak correlation between total rainfall from a single water year and the following summer's peak ΔSLI is perhaps unsurprising. After all, some aspects of the hydrology and mechanics of large landslides, like maximum annual water levels (Iverson & Major, 1987) and multiyear average velocity (Bennett, Roering, et al., 2016), may be relatively insensitive to short-term changes in surface water balance and instead have response timescales >1 year. The strong positive relationship between three-year cumulative rainfall and July ΔSLI could reflect the response time of the shallow soil moisture reservoir upon which annual grassland vegetation depends. At steady state, the residence time, and hence response timescale, of water within the earthflow body can be estimated by dividing porosity-weighted earthflow thickness by annual rainfall rate. For a porosity of 0.44 and earthflow thickness of 8 m (Murphy et al., 2018), the annual rainfall of ~0.5 m (PRISM, 2017) yields a response time of ~7 years. Given that the near-surface soil moisture reservoir upon which annual grasslands depend should be a smaller volume than the entire earthflow body, a three-year response time for shallow moisture is plausible.

Lastly, these data suggest that the magnitude of the spectral bathtub effect (peak annual ΔSLI) is linked to landslide movement. Two and a half years of continuous daily GPS positions from the transport zone of Oak Ridge earthflow (Finnegan & Nereson, 2017) show that it moved farther during the water year characterized by the

larger spectral bathtub effect. In 2016, total annual displacement and peak ΔSLI were 6 cm and 0.12, respectively. In 2017, they were 46 cm and 0.18. Time series of GPS positions are published on the website of the Nevada Geodetic Laboratory (http://geodesy.unr.edu/NGLStationPages/stations/OREO.sta).

2.8 Conclusions

These results indicate that entrapment of water in persistently active landslides with low-permeability boundaries can be remotely sensed via its coupling to shallow soil moisture and vegetation health. At Oak Ridge earthflow, spectral indices suggest that the landslide was perennially wetter, which had ecological consequences as vegetation thrived for longer into the summer dry season. Our proxy for soil moisture contrast (i.e., the bathtub effect) was correlated with multiyear rainfall totals and its magnitude diminished to zero after three years of drought (suggesting draining of the bathtub), before rebounding in subsequent, above-average rainfall years. This type of analysis could be scaled to monitor many landslides simultaneously at low cost. If consistent relationships between spectral indices, water levels, and displacement can be established, such monitoring could be useful in forecasting landslide movement in the future.

2.9 Acknowledgements

This work was supported by a National Science Foundation (NSF) Graduate Research Fellowship awarded to A. Nereson and NSF grants Geomorphology and Land Use Dynamics Program EAR-1658800 and EAR-1613122 to N. Finnegan. Further support came from the Casey Moore Fund (UC Santa Cruz) and from Northern California Geological Society's Richard Chambers Memorial Scholarship in awards to A. Nereson. We thank the San Francisco Public Utilities Commission and Russ Fields for site access. We also thank Georgina Bennett and one anonymous reviewer for helpful comments on this manuscript. Data from all plots can be found in the supporting information. Time series of GPS positions referenced in text are published on the website of the Nevada Geodetic Laboratory (http://geodesy.unr.edu/NGLStationPages/stations/OREO.sta).

Chapter 3.

Patterns of rainfall, pore pressure response, and displacement at Oak Ridge earthflow, California

3.1 Abstract

Here we present 2.5 years of high-temporal resolution (10 minute) pore-water pressure and daily GPS data for a seasonally-active earthflow in California's northern Diablo Range. We found no discernable pore-water pressure response at 2-3 m depth for the first ~2 months following the onset of seasonal precipitation, regardless of the magnitude, duration, or intensity of the rainfall events during those periods. When pore-water pressures finally responded, they did so abruptly and with a magnitude larger than could be accounted for based on the year-to-date cumulative rainfall; and earthflow movement commenced shortly thereafter. These data offer indirect evidence for an effect described by Gillham (1984), in which the addition of a relatively small amount of rainfall to a zone of tension saturate can trigger a rapid and highly disproportionate rise in the water table. Moreover, they suggest that simple, one-dimensional linear diffusion models are not physically-appropriate for characterizing the lag between the onset of seasonal precipitation and pore-water pressure response/landslide motion at our site. These results may also apply to other earthflows that develop a substantial unsaturated zone just below ground surface.

3.2 Introduction

Intermittent movement of deep-seated (>5 m), slow-moving (<10 m/a) landslides is a common phenomenon with important scientific and practical implications. These landslides, often referred to as earthflows (Hungr et al., 2014), can dominate erosion in mountainous landscapes (Mackey and Roering, 2011), control the long-term evolution of catchment geometry(Booth et al., 2013), and cause progressive damage to infrastructure and property over time (Bertolini et al., 2005).

The role of earthflows in shaping landscapes is amplified by their longevity. Historical observations demonstrate that intermittently active earthflows can persist for decades or centuries (e.g. Crandell and Varnes, 1961; Bovis, 1985; Mackey et al., 2009; Roering et al., 2015; Del Soldato et al., 2018), while geologic and geochronologic evidence further suggests that some may be active for millennia (e.g. Bovis and Jones, 1992; Madole, 1996; McSaveney and Griffiths, 1987). At these long timescales, the periodicity of earthflow movement is largely regulated by factors such as weathering rates and the supply of mobile regolith (Mackey and Roering, 2011), climate change (Bennett et al., 2016), or base level variations due to river incision or aggradation at earthflow toes (Bilderback et al., 2014).

At shorter timescales, earthflow movement is regulated by precipitation-driven changes in pore-water pressure at the basal shear surface (Terzaghi, 1950; Baum et al., 2003; Iverson, 2000, 2005). Annual cycles of movement in response to seasonal rainfall are commonly reported (Kelsey, 1978; Keefer and Johnson, 1983; Iverson and Major, 1987; Hilley et al., 2004; Handwerger et al., 2013). Despite many studies

on the topic, however, it remains difficult to identify reliable rainfall amounts or pore-water pressures sufficient to cause seasonal earthflow accelerations or to predict post-failure velocities (e.g. Angeli et al., 1996; Picarelli et al., 2004; Van Asch, 2005; Schulz et al., 2009, 2018). That said, quantifying the interaction between rainfall and earthflow mobility is critical to assessing the impact these features will have on people and landscapes in the future.

Many studies have suggested that transient pore-water pressure changes resulting from rainfall are transmitted from the surface to depth in the vertical direction and are well described by a one-dimensional linear diffusion equation (Iverson and Major, 1987; Haneberg, 1991; Reid, 1994; Iverson, 2000; Berti and Simoni, 2010). In this framework, the minimum time required for a rainfall pulse to manifest as a 'strong' pore-water pressure change at the slide base is: $T_D = Z^2/D_o$, where Z is landslide thickness below the water table and D_o is the characteristic hydraulic diffusivity (Iverson, 2000; Coe, 2012). Because these models are simple, accessible, and require few input parameters, they often ignore many complexities, including variable saturation, heterogeneous hydraulic properties, surface ponding, and preferential flow pathways. Nevertheless, they have proven successful in accounting for the hydrologic and mechanical response of slow landslide material in many settings, particularly when applied during the peak wet season, when soils are often saturated, or nearly saturated (or assumed to be so), and thus D_o ought to be more constant in space and time (e.g. Reid, 1994).

A first-order observation of intermittent earthflow behavior is that the onset of seasonal earthflow acceleration typically lags behind the onset of precipitation by weeks to months (Iverson and Major, 1987; Handwerger et al., 2013; Cohen-Waeber et al., 2018). While it is tempting to interpret this initial lag as the characteristic timescale, T_D, defined from the one-dimensional, linear diffusion models, the relationship is problematic. For example, with these models, hydro-mechanical response time of landslides should scale with landslide thickness. However, Handwerger et al. (2013) found no detectable differences in response times between the onset of motion of 10 earthflows in California's Eel River catchment, despite a five-fold variation in their inferred thicknesses (8-40 m). Moreover, they noted that all the earthflows accelerated within 40 days of the onset of seasonal rainfall, which was substantially faster than estimated for even the thinnest landslide, assuming a characteristic hydraulic diffusivity value of 10^{-6} m^2/s (Iverson and Major, 1987). Instead, they offer several possible resolutions to this apparent conflict: (1) the landslides are sensitive to subtle hydrologic perturbations (i.e. a 'strong' pressure change isn't required at depth for acceleration and therefore response times can be shorter), (2) the 'effective' diffusivity governing landslide behavior is much higher than field-derived values (Iverson and Major, 1987), possibly due to piping through macro-pores, and (3) a simple, one-dimensional diffusion model might not be appropriate for these three-dimensional, time-dependent systems.

Handwerger et al. (2013) did not directly address another possible explanation for this type of behavior that was described 20+ years prior. At Minor Creek landslide in

California, Iverson and Major (1987) observed abrupt, early-season pressure head increases during one winter that would have required >3 times the year-to-date rainfall to fill empty pore space in the soil. Consequently, they inferred that "transient groundwater responses early in the wet season can be influenced strongly by antecedent water storage in the unsaturated zone, whereas responses later in the wet season are directly related to pore pressure transmission that accompanies saturated groundwater flow." This observation was compared to the effect first described by Gillham (1984), who demonstrated that shallow water tables can respond in a highly disproportionate manner to small precipitation events if they interact with a previously-established, tension-saturated, capillary fringe. In loamy soils characteristic of earthflow-prone landscapes (e.g. Brown and Ritter, 1971) capillary rise may dampen soil several meters above the water table (Fetter, 2001). Therefore, precipitation might only need to migrate from the ground surface down to the top of the tension-saturated zone (which could be coincident with the ground surface for some earthflows) in order to trigger a rapid change in the position of the water table.

Here we present 2.5 years of high-temporal resolution (10 minute) pore-water pressure and daily GPS data for a seasonally-active earthflow in California's northern Diablo Range. We found no discernable pore-water pressure response at 2-3 m depth for the first ~2 months following the onset of seasonal precipitation, regardless of the magnitude, duration, or intensity of the rainfall events during those periods. When pore-water pressures at depth finally responded, they did so abruptly and with a magnitude larger than could be accounted for based on the year-to-date cumulative

rainfall; and earthflow movement commenced shortly thereafter. These data offer indirect evidence for the presence of a tension-saturated zone and that simple, one-dimensional linear diffusion models are not physically-appropriate for characterizing the lag between the onset of seasonal precipitation and pore-water pressure response/landslide motion at our site. These results may also apply to other earthflows that develop a substantial unsaturated zone just below ground surface.

3.3 Study Area

Oak Ridge earthflow is a seasonally active landslide in the northern Diablo Range, 20 km northeast of San Jose, California (Fig. 1a). It is 1.8 km long (area=0.35 km^2), spans 600 m of relief, and has average slope of 17°. In its fastest section (the transport zone), Oak Ridge earthflow moved >275 m between 1937 and 2017. Velocity during this period was linked to variability in surface moisture balance and upslope sediment supply (Nereson and Finnegan, 2018). Local bedrock consists of the Mesozoic-early Cenozoic Franciscan Complex (Rubin, 2002). Franciscan lithologies are dominated by metamorphic sandstones and mudstone mélanges and are highly susceptible to hillslope failure and earthflow processes (Kelsey, 1978; Keefer and Johnson, 1983; Mackey and Roering, 2011; Handwerger et al., 2013; Scheingross et al., 2013).

Oak Ridge earthflow is subject to a Mediterranean climate, with hot, dry summers and mild, wet winters. Average annual precipitation is 52.7 cm (20.7 in) and falls mainly as rain between the months of October and April (PRISM Climate Group,

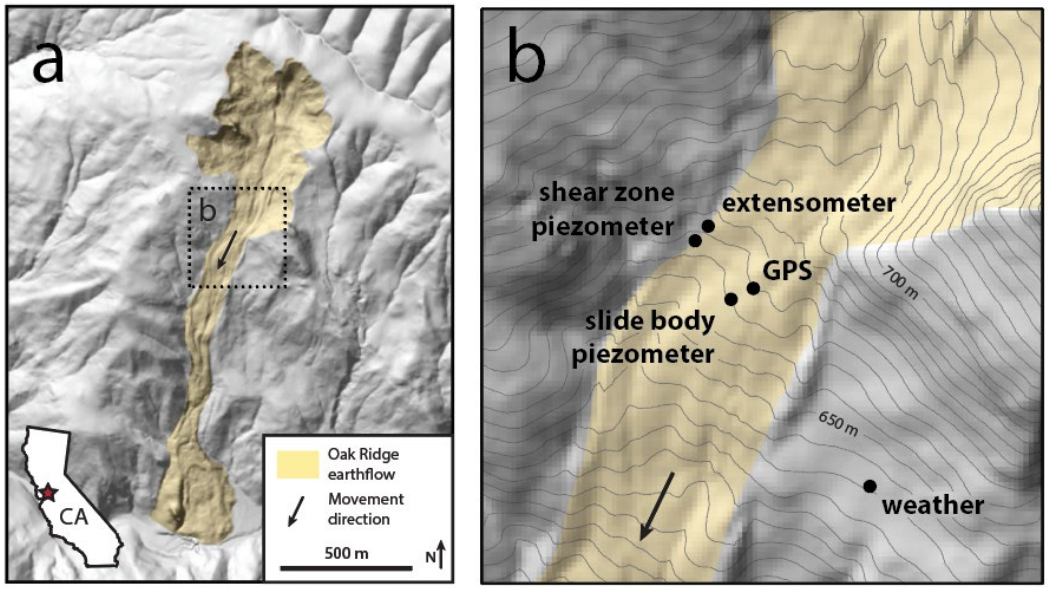

Figure 3.1. (a) Extent of Oak Ridge earthflow. (b) Inset with locations of instrumentation; 5-meter contours.

2017). Vegetation is primarily non-native annual grassland, with some oak savanna, mixed evergreen woodland, and minor amounts of Diablan sage scrub (SFPD, 2008).

The grain size analyses of Nereson et al. (2018) indicate that the earthflow body consists of loamy soil with the following average weight distribution: 24% gravel, 38% sand, 26% silt, 12% clay. Atterberg limits indicate that the fine fraction is made up of low-plasticity silts and clays. Samples taken adjacent to the lateral shear zone are enriched in silt and clay relative to the earthflow body (average distribution: 17% gravel, 28% sand, 38% silt, 17% clay) and are characterized as low-plasticity clay, but with liquid limits that are approximately twice as large as samples from the slide body. Hydraulic conductivity was estimated to be ~two orders of magnitude smaller in the shear zone ($2.6*10^{-6}$) than in the slide body ($4.4*10^{-4}$ m/s). The residual friction angle of shear zone material was determined by ring shear tests to be 12-14°.

3.4 Methods

We measured rainfall, pore-water pressure, and landslide displacement within the upper transport zone of Oak Ridge earthflow (Fig. 1) over a period of 2.5 years. At least seventy-two meters of downslope motion has occurred in this zone over the past 80 years (0.9 m/yr), with large annual displacements measured in remotely-sensed imagery as recently as 2006 (Nereson and Finnegan, 2018).

3.4.1 Rainfall

We recorded rainfall, along with temperature, atmospheric pressure, and relative humidity in 10-minute intervals using a sensors manufactured by Onset corporation and stored using their Hobo Micro Station Data Logger. All weather station components were mounted on <2 m above the ground surface on a stable hillslope adjacent to the earthflow (Fig. 1). The rainfall sensor had a tipping bucket mechanism that summed rainfall in 2 mm increments over each 10-minute recording interval.

Individual rainfall events in this record were initially defined as continuous periods of rainfall separated by at least 24 hours from other events. These rainfall events were then compared to pore-pressure responses. In cases where a single rainfall event contained multiple 'bursts' that were clearly associated with pressure sensor responses of their own, we divided them into separate events (Fig. 2). Here, the term 'pressure sensor response' indicates the short-term increase of pressure head recorded by a piezometer in response to a specified rainfall event and is superimposed on the long-wavelength seasonal pressure signal (Berti and Simoni, 2010).

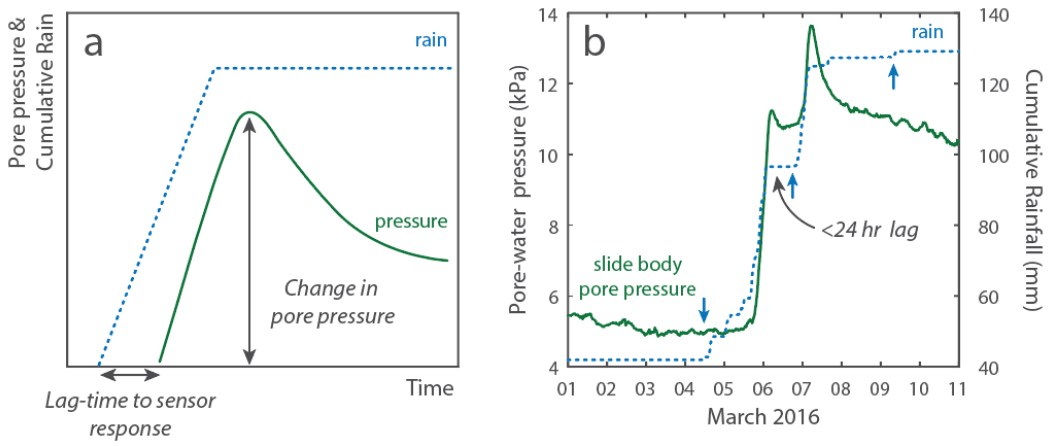

Figure 3.2. (a) Schematic rainfall event and associated pore-water pressure response. (b) Example data showing three rainfall events (blue arrows) and associated slide-body pressure response. Note that the middle rainfall event began less than 24 hours after the end of the previous event. However, since it triggered a clear increase in pore-water pressure separate from the first, we defined it as a separate event.

3.4.2 Pore-water pressure

We recorded pore-water pressure in 10-minute intervals using vibrating-wire piezometers (RST Instruments, model VW2100-0.07) installed at two locations. One was located in the western lateral shear zone of the earthflow and one was located approximately 50 m away, in the central portion of the earthflow body. Final sensor depths were 2.71 m and 2.52 m below the ground surface, respectively. Boreholes were manually excavated with a hand auger and backfilled with a grout slurry composed of water, cement, and bentonite (weight ratio = 2.49 : 1.00 : 0.41). This method is known as the 'fully-grouted' method of installation and is encouraged for vibrating wire piezometers (Contreras et al., 2008). Piezometers were attached to single-channel data loggers and programmed to record fluid pressures ≤70 kPa with an accuracy of 0.07 kPa at 10-minute intervals. Piezometer readings were corrected

for changes in ground temperature and atmospheric pressure using a linear calibration provided for each sensor by the manufacturer.

3.4.3 Earthflow displacement

To measure displacement of Oak Ridge earthflow, we installed a continuous GPS station atop a large boulder in the upper transport zone near the slide-body piezometer (Fig. 1b). We used a Trimble NetR9 receiver and a Trimble GNSS Zephyr antenna. Post processing of GPS data was conducted at the Nevada Geodetic Laboratory (Blewitt et al., 2013) and daily time series of positions are published online (http://geodesy.unr.edu/NGLStationPages/stations/OREO.sta). Positions were calculated in the NA12 terrestrial reference frame, which typically has a precision of 1.0 mm in the north, 0.9 mm east, and 3.4 mm in the vertical components (Blewitt et al., 2013). Daily GPS positions were converted to daily displacements (average daily velocity) by first subtracting background plate tectonic motion (~1.7 cm/yr towards the northwest), which was determined to be within ~one order of magnitude of earthflow motion, using data from two nearby permanent GPS stations installed on stable slopes (see SI). We then calculated the time derivative of tectonically-corrected positions in the direction of earthflow motion (determined using the azimuth of the best-fit line to the 2017 tectonically-corrected daily positions).

For the last six months of our monitoring period, we also recorded earthflow displacement using a vibrating-wire extensometer (RST Instruments, model EXSR-1300) that spanned the active earthflow margin, approximately two meters away from

the shear zone piezometer (Fig. 1). The extensometer was buried to a depth of 20 cm and the long axis was oriented as close to parallel to the strike of the slickensided shear zone as possible, with the flanges located diagonally across from one another. The lateral shear face became exposed in April 2017 when a >250 m-long (<5 cm wide) fissure opened along its length as earthflow soil began to desiccate and crack (Nereson and Finnegan, 2018). Undecomposed roots of annual grasses along the shear surface were preferentially oriented in the direction of downslope movement, which indicated that this was the active shear zone in 2017. The extensometer was set to log data every 10 minutes, with a resolution of 0.06 mm and an accuracy of 0.75 mm. Measurements were compensated for the geometry of the installation (the extensometer was oriented ~13° off strike of the shear plane) and for temperature variability using a linear calibration provided by the manufacturer to yield displacement in the downslope direction.

3.5 Results

3.5.1 Seasonal patterns of rainfall, pore-water pressure, and displacement

Two and a half years of monitoring data from Oak Ridge earthflow reveal coupled relationships between rainfall, pore-water pressure, and earthflow displacement at variable timescales, from an entire season to single rainfall events. We began collecting data on January 27, 2016, four months after the start of water year 2016 (water year (WY) = October 1st – September 30th) and more than halfway through the typical rainy season (October-April). For a clear description of annual

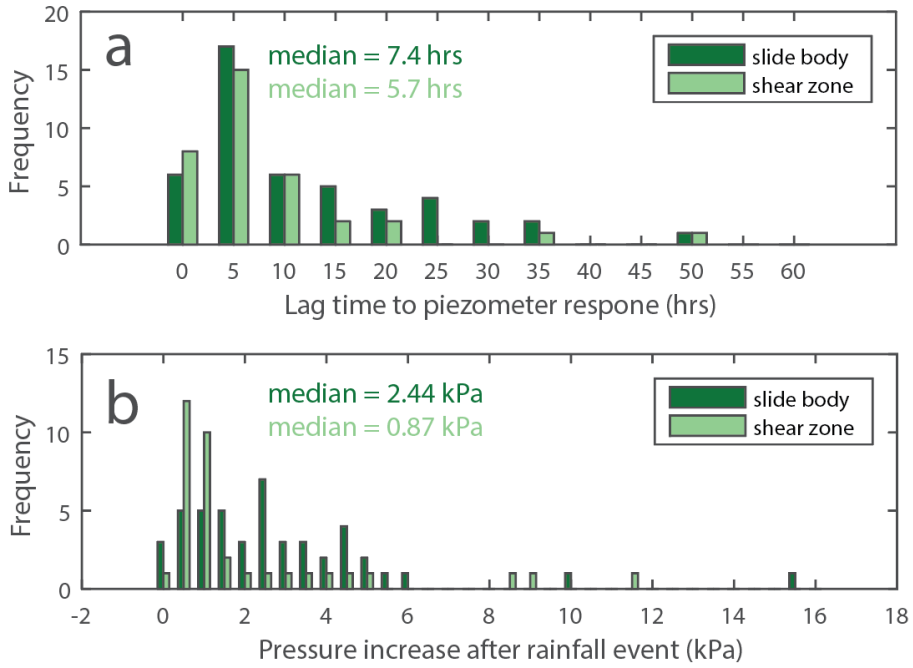

Figure 3.3. Histograms of (a) lag time to piezometer response and (b) pressure increase per rainfall event. Data include all years 2016-2018.

patterns, we begin here with WY 2017, the first water year for which we have complete instrumental records.

On October 14, 2016, the first rainfall event of the season began, breaking a five-month-long dry spell during which no measureable rain fell (Key Event 1, Fig. 2a). At this time, pore-water pressures at both piezometers were negative and on decreasing trajectories, indicating that the water table was >2.5 m below the ground surface and dropping deeper over time (Fig. 2b). GPS data show that the earthflow had come to a full stop three months prior to this event and that no measureable displacement had occurred during the intervening period (Fig. 2d).

Over the next 57 days, 150.2 mm of rain fell during 12 individual rainfall events. Despite this accumulation (~18% of the WY 2017 total), there was there was no

discernable pore-water pressure response in either piezometer; pressure head at both locations continued to decrease and the earthflow remained stationary. However, on December 9th, 2016, less than 24 hours after the onset of the 13th rainfall event, both piezometers began to record a large increase in pressure that continued until the next rainfall event four days later (Key Event 2, Fig. 2b-c). In sum, these two rain events triggered an increase in pore-water pressure of >20 kPa in each piezometer, or ~80% of the total annual variability measured during WY 2017. During one 16-hour period, pore-water pressures in the slide body rose from negative values to 9.88 kPa, which is the pressure equivalent of about one meter of water above the sensor. The earthflow remained stationary throughout this increase in shallow pore-water pressure.

Following Key Event #2 (Fig. 2b-c), we recorded 23 additional rainfall events of varying durations and magnitudes during WY 2017. Most rainfall events were followed by shallow pore-water pressure responses in both piezometers that had relatively short median lag times (4-7 hours) between the onset of rainfall and the first clear pore-water pressure increase at the sensor depth (see Fig. 3). These rapid responses were two orders of magnitude faster than the 57-day lag time between the first rainfall event of the season and the first pore-water pressure response.

On January 7th, 2017, 84 days after the onset of rainfall and 27 days after the first pore-water pressure response, the earthflow exhibited its first unambiguous acceleration of WY 2017 (Key Event #3, Fig. 2d). The pore-water pressure in the slide body at the start of motion was 8.99 kPa. After this initial acceleration, the earthflow continued to move for the next ~230 days with an average velocity of 2.0

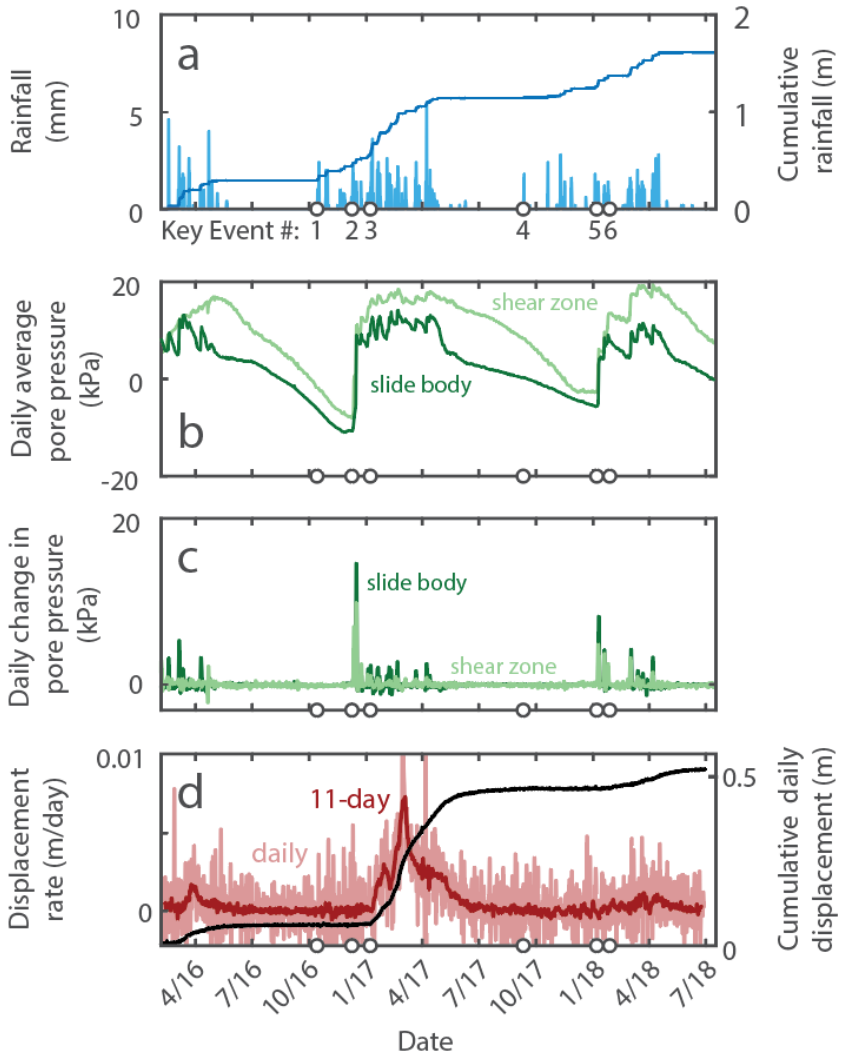

Figure 3.4. Time series of (a) rainfall, (b-c) pore-water pressure, and (d) GPS displacement at Oak Ridge earthflow for the period of January 27, 2016 until July 17, 2018. White dots indicate the timing of the following key events in water years 2017 and 2018: first seasonal rainfall, first pore-water pressure increase, and first unambiguous landslide acceleration.

mm/day and a maximum velocity of 13 mm/day on February 22nd, 2017. Around May 8th, 2017, the earthflow experienced marked deceleration that resulted in full cessation of motion by August 26th, 2017 at a slide body pore-water pressure of 0.66 kPa. During its nearly eight months of activity in WY 2017, the earthflow moved a total of 46.4 cm.

Water year 2018 was characterized by a similar succession of events to those just described. Seasonal precipitation began on September 11, 2017 (Key Event #4, Fig. 2a), just a few weeks after the earthflow had completely stopped moving from the previous year. On that date, pore-water pressure in both piezometers was low and decreasing every day, including into negative values (Fig. 2b). Over the next 119 days, 120.2 mm of rain fell during 13 rain events (~26% of the WY 2018 total). Again, no pore-water pressure response was discernable during this time and no earthflow motion was detected.

On January 9th, 2018, approximately one day after the 14th rain event of the season, both piezometers began recording a large increase in pressure within 24 hours of one another (Key Event #5, Fig. 2b-c). The total increase in pore-water pressure associated with this event was smaller than the initial increase we observed in 2017 (compare Key Event #'s 2 and 5 in Fig. 2c), but was still larger in magnitude than any subsequent response and accounted for a disproportionate amount (~40-55%) of total pressure variability in WY 2018. Following Key Event #5, we recorded 18 additional rainfall events. The median lag time between the onset of these subsequent rain events and their associated pore-water pressure responses was short (6-7 hours). Again, this behavior stands in sharp contrast to the prior 119 days, during which there was no detectable increase in pore-water pressure.

On January 29, 2018, ~139 days after the onset of rainfall and ~20 days after the first pore-water pressure response, the earthflow began to accelerate gradually (Key Event #6, Fig. 2d). The pore-water pressure in the slide body at the start of motion

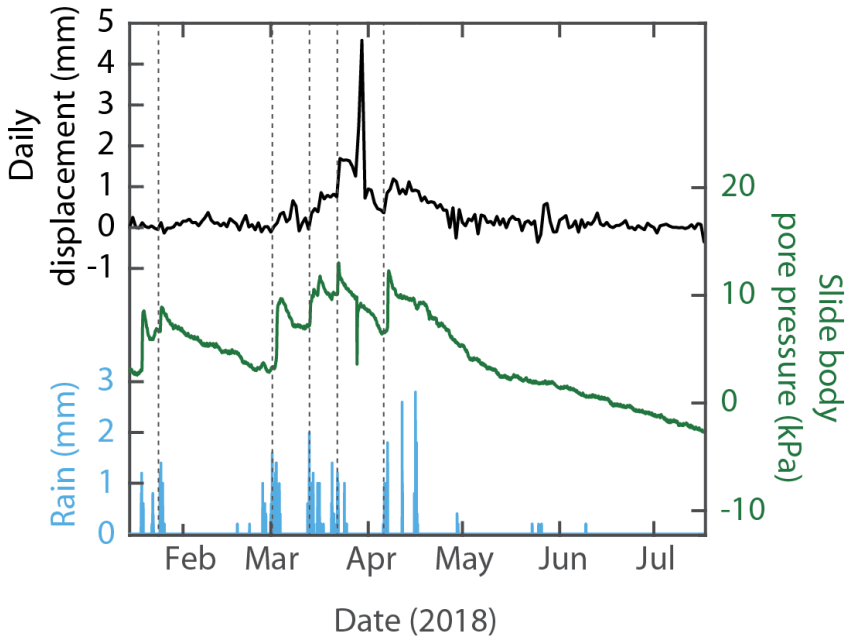

Figure 3.5. Daily displacement as derived from extensometer measurements (black), change in slide-body pore-water pressure (green), and 10-minute precipitation totals (blue) for the period of January 15, 2018 until July 17, 2018. Dashed lines indicate pore-water pressure increases of >1 kPa in a 24-hour period.

was 7.68 kPa. After this initial acceleration, the earthflow continued to move for the next ~152 days with an average velocity of 0.38 mm/day and a maximum velocity of 0.47 mm/day on March 4th, 2018. Around April 29, 2018, the earthflow clearly started to decelerate and motion was trivial by the end of our data collection on July 17, 2018. During its approximately five months of activity in WY 2018, the earthflow moved a total of 58 mm.

3.5.2 Individual rainfall events and earthflow acceleration

For the six-month period from January 15, 2018 until July 17, 2018, the vibrating wire extensometer recorded displacement along the western lateral shear zone with a

precision about one order of magnitude greater than the continuous GPS station. In the time since it was installed, the extensometer recorded 56.3 mm of downslope displacement, which is in remarkable agreement with the displacement measured at the GPS station during WY 2018 (58 mm, Fig. 3). Additionally, this data provides useful insights into the coupling of rainfall, pore-water pressure, and displacement at the scale of individual rainfall events.

For each rainfall event that generated an increase in pore-water pressure in the slide body of >1 kPa within a 24-hour period, we see a corresponding acceleration of earthflow displacement that commenced within about one day of the onset of rainfall (Fig. 3).

3.6 Discussion

Handwerger et al. (2013) used a linear, one-dimensional diffusion model to calculate the time it would take for pressure pulses generated at the surface to diffuse to the base of earthflows of various sizes in order to initiate seasonal motion. A key finding of this analysis is that for the hydraulic diffusivities in the range reported by Iverson and Major (1987), a simple diffusion model is unable to explain the apparently uniform start times of slow landslides throughout northern California despite their wide range of depths. This result is surprising because landslides of different depths that are subjected to the same pressure forcing at the surface should respond at different times and with different sensitivities, owing to the attenuation of the surface-generated pressure pulse.

Our results, however, imply that the seasonal onset of motion of Oak Ridge earthflow is not governed primarily by diffusion of rainfall generated pore-water pressures at the surface. Rather, we see a 3-5 month lag time between the onset of seasonal rainfall and of landslide motion, much of which is characterized by negative pore-water pressures at depths of ~2.5 m, implying unsaturated or tension-saturated conditions there. Additions of rainfall during these periods generated no positive pressure pulses in the ground below ~2.5 m, indicating that much of the water likely went into near-surface soil moisture storage.

Starting with Key Event #s 2 and 5 (Fig. 2b-c), we saw large increases in pore-water pressure over relatively short periods of time that were much greater than what would be generated by the cumulative total of seasonal rainfall (Key Event #s 2 and 5, Fig. 2b-c). Given the 2017 water year-to-date rainfall total of 150.2 mm and an estimated slide body porosity of 0.44 (Nereson et al., 2018), we could have expected an increase to positive 3.35 kPa at most, assuming fully unsaturated conditions. Instead, these rapid rises in pressure, which amounted to >20 kPa and marked the transition from negative to positive pressures, account for highly disproportionate amounts ~40-80% of overall seasonal variability and are followed relatively shortly by the onset of earthflow motion (Key Event #s 3 and 6, Fig. 2d). This implies that the vadose zone processes that govern the retention and release of shallow, unsaturated soil moisture are the key control on the onset of seasonal landslide motion in such settings.

Gillham (1984) demonstrated that the addition of a very small amount of water to the top of a tension-saturated zone (capillary fringe) can result in an immediate and highly disproportionate rise in the water table as water formerly held in tension is released. In Gillham's (1984) experiment, the addition of 0.3 cm of water to a tension-saturated sand resulted in a water table rise of 30 cm in 15 seconds. The rapid increases in pore pressure during Key Event #s 2 and 5 (Fig. 2b-c) are evocative of such behavior (1984), for example, during Key Event #2, pore-water pressures in the slide body rose from negative values to +9.88 kPa (~1 meter of water) in less than sixteen hours.

Iverson and Major (1987) also noted a particularly rapid rise in pore-water pressure (of a similar disproportionate magnitude (1-2 m) to the ones we report here) that lagged behind precipitation and triggered the onset of seasonal motion during one year at the Minor Creek landslide in northern California. However, in their case, the soil was fully saturated at the sensor depth (3-6 m) when the pore pressure rise began, so it was more speculative to assume the presence of a tension-saturated zone. Moreover, their weekly pressure sampling rate and averaging of multiple wells made it difficult to assess how rapidly their pore pressure increase occurred. That said, Iverson and Major (1987) nevertheless suggest that their observation may be linked to the capillary fringe effect described by Gillham (1984).

Additionally, Berti and Simoni (2010) report data from another active earthflow in a Mediterranean climate with abrupt pressure head signals that arrive at shallow (<3 m) sensors throughout the wet season. The bulk of these signals cannot be

attributed to the capillary fringe effect described by Gillham (1984), because they occur under largely saturated conditions with positive pore-water pressures. That said, at least one of their sensors records rapid and disproportionately large (>75% of annual variability) pressure increases from values of near-zero to ~40 cm of head near the start of the wet season. Berti and Simoni (2010) consider this well's behavior to be anomalous, but it is similar to the behavior of our piezometers and could be another case where the capillary fringe plays an outsized role in the magnitude of the initial pressure response.

Given these observations and the difficulty that Handwerger et al. (2013) noted in using one-dimensional, linear pore-water pressure diffusion to model the onset of motion for earthflows, we propose that the effective diffusivities reported or modeled for slow landslides in northern California in fact reflect the timescale associated only with the transit of relatively small amount of soil moisture through—or perhaps the saturation of—the comparatively thin unsaturated zone to the top of the tension-saturated zone. After this saturation occurs, a large change in water table depth can occur over short periods of time (minutes to hours).

Notably, the timescale associated with saturating the surface soil reservoir should have no implicit depth dependence, except what is determined by the depth of the capillary fringe below the ground surface, which does not directly depend on total landslide depth. Because the ability of a soil to conduct water decreases drastically as water content decreases (Freeze and Cherry, 1979), it may take a few months for rainfall to saturate or for a small amount to percolate through that dry, uppermost

layer. This may be why some previous studies like that of Iverson and Major (1987) have required low (10^{-6}) diffusivities to explain the initial lag (~75 days for a 6-meter-deep landslide) between the onset of seasonal precipitation and motion. In contrast, the behavior of earthflows that respond relatively quickly (<40 days for a 40-meter-deep landslide, Handwerger et al. (2013)) and have relatively high effective diffusivities (10^{-4}) may be explained in this framework in a number of ways. For example, the top of the capillary fringe may be located closer to the surface at these earthflows as a result of textural and structural characteristics of the soil material (capillary rise height inversely correlated with grain size in many natural soils); or the presence of effective hydrological barriers in the basal and lateral shear zones of an earthflow could allow it to maintain shallow water tables (and thus shallow-er capillary fringes) year-round (Baum and Reid, 2000).

Alternatively, or likely in addition to these options, the amount of antecedent soil moisture in the unsaturated zone at the start of the rainy season would also be a critical factor in determining the transit time of water from the ground surface to the top of the capillary fringe, given the non-linear dependence of hydraulic conductivity on soil water content and hydraulic head. In any case, we argue that the initial lag between seasonal rainfall and earthflow motion is not diffusive in nature, even though late-season pressure pulses likely do migrate diffusively and more rapidly through earthflow bodies under saturated or near-saturated conditions (Iverson and Major, 1987; Haneberg, 1991; Reid, 1994; Berti and Simoni, 2010) (Fig. 3).

In support of this interpretation, following the onset of positive pore fluid pressures at Oak Ridge earthflow, we see a tight correspondence between rainfall events and shallow pore fluid pressure responses (Figs. 2a-c and 3). From these events, we calculated values of effective hydraulic diffusivity using the depth of the pore pressure sensors and the median lag time between the onset of rainfall events (Fig. 5) and their corresponding pore-water pressure responses. We calculate average diffusivities of 2.4 $*10^{-4}$ to 3.6 $*10^{-4}$ m^2/s. This range of values is similar to those determined experimentally by Berti and Simoni (2010), but is ~ 2 orders of magnitude larger than the widely cited diffusivities reported by Iverson and Major (1987) for the Minor Creek landslide. The relatively efficient diffusion of pore pressure at Oak Ridge is also supported by the tight correspondence between shallow pore-water pressure and landslide motion (Fig. 3). A diffusivity of 10^{-5} or 10^{-6} would imply diffusion timescales of months to years to get to the estimated depth of the detachment (8 m, Murphy et al., 2018). The magnitude of this time lag is clearly inconsistent with the results of our analysis, which shows earthflow accelerations clearly within two days of rainfall events.

3.7 Conclusions

The use of simple one-dimensional, linear diffusion models for the transient fluctuations of pore-water pressure in landslides has been important in growing our understanding of earthflow movement and can be used to characterize a wide variety of landslide styles and rates (Iverson, 2000). Those who have successfully applied

them are typically careful to point out that they are best used when hydraulic diffusivity can be assumed to be constant in space and time. This is most certain to be the case under saturated conditions, because unsaturated hydraulic conductivity (on which diffusivity closely depends) varies greatly and non-linearly with variations in water content and hydraulic head.

It has nevertheless remained tempting to use these models to estimate and explain variability in the lag time between the onset of seasonal rainfall and the first seasonal acceleration of earthflows (Handwerger, et al., 2013). Here, we have argued that the effective diffusivity calculated from that lag time conflates (1) non-diffusive (and/or non-*linearly* diffusive) processes in the vadose zone, including those that may result from the interaction of rainfall with the capillary fringe, and (2) authentic linear pore-pressure diffusion below the water table. Given the abundance of earthflows in areas with well-defined rainy seasons separated by hot, dry summers (e.g. California and Italy), many of these landslides likely develop an unsaturated zone through which the effects of rainfall must be filtered. Additionally, since the thickness of the capillary fringe does not depend directly on landslide thickness, the time it takes for rainfall to migrate through the near-surface unsaturated zone (which in turn is influenced by its thickness, texture, and ambient moisture content at the start of the rainy season) may be the dominant factor in estimating the onset of motion for landslides like Oak Ridge earthflow.

References

Allen, B. (2016). Groundwater Recharge of a Landslide : An Isotopic and Meteorological Analysis. Portland State University.

Angeli, M.-G., Gasparetto, P., Massimiliano Menotti, R., Pasuto, A., and Silvano, S., 1996, A visco-plastic model for slope analysis applied to a mudslide in Cortina d'Ampezzo, Italy: Quarterly Jounral of Engineering Geology, v. 29, p. 233–240.

ASTM, I. (2008). Annual book of ASTM standards, 4.08. Philadelphia, PA: American Society for Testing and Materials.

Baret, F., Jacquemoud, S., & Hanocq, J. F. (1993). The soil line concept in remote sensing. Remote Sensing Reviews, 7, 65–82. https://doi.org/10.1016/0273-1177(93)90560-X.

Baum, R. L., & Fleming, R. W. (1991). Use of longitudinal strain in identifying driving and resisting elements of landslides. Geological Society of America Bulletin, 103(8), 1121–1152. https://doi.org/10.1130/0016-7606(1991)103<1121:UOLSII>2.3.CO;2

Baum, R. L., and Johnson A.M., 1993, Steady movement of landslides in fine-grained soils—A model for sliding over an irregular slip surface, U.S. Geological Survey Bulletin, 1842-D, 28 p.

Baum, R.L., and Reid, M.E., 2000, Ground water isolation by low-permeability clays in landslide shear zones, in Bromhead, E., Dixon, N., and Ibsen, M. eds., Landslides in Research, Theory and Practice, Proceedings of the 8th International Symposium on Landslides, London, p. 139–144.

Baum, R.L., Savage, W.Z., and Wasowski, J., 2003, Mechanics of Earthflows, in Picarelli, L. ed., Proceedings of the International Workshop on Occurence and Mechanism of Flow-Like Landslides in Natural Slopes and Earthflills, Associazione Geotechnica Italiana, Sorrento, Italy, p. 1–8.

Bennett, G.L., Miller, S.R., Roering, J.J., Schmidt, D.A., 2016, Landslides, threshold slopes, and the survival of relict terrain in the wake of the Mendocino Triple Junction: Geology; v. 44, p. 363–366, doi: https://doi.org/10.1130/G37530.1.

Bennett, G.L., Roering, J.J., Mackey, B.H., Handwerger, A.L., Schmidt, D.A., and Guillod, B.P., 2016, Historic drought puts the brakes on earthflows in Northern

California: Geophysical Research Letters, v. 43, p. 5725–5731, doi: 10.1002/2016GL068378.

Berti, A., and Simoni, M., 2010, Field evidence of pore pressure diffusion in clayey soils prone to landsliding: Journal of Geophysical Researchy, v. 115, p. 20, doi: 10.1029/2009JF001463.

Bertolini, G., Guida, M., and Pizziolo, M., 2005, Landslides in Emilia-Romagna region (Italy): Strategies for hazard assessment and risk management: Landslides, v. 2, p. 302–312, doi: 10.1007/s10346-005-0020-1.

Bilderback, E.L., Pettinga, J.R., Litchfield, N.J., Quigley, M., Marden, M., Roering, J.J., and Palmer, A.S., 2014, Hillslope response to climate-modulated river incision in the Waipaoa catchment, East Coast North Island, New Zealand: Geological Society of America Bulletin, p. 0–18, doi: 10.1130/b31015.1.

Booth, A.M., and Roering, J.J., 2011, A 1-D mechanistic model for the evolution of earthflow-prone hillslopes: Journal of Geophysical Research, v. 116, doi: 10.1029/2011JF002024.

Booth, A.M., Roering, J.J., and Rempel, A.W., 2013, Topographic signatures and a general transport law for deep-seated landslides in a landscape evolution model: Journal of Geophysical Research: Earth Surface, v. 118, p. 1–22, doi: 10.1002/jgrf.20051.

Bovis, M.J., 1985, Earthflows in the Interior Plateau, southwest British Columbia: Canadian Geotechnical Journal, v. 22, p. 313–334, doi: 10.1139/t85-045.

Bovis, M.J., and Jones, P., 1992, Holocene history of earthflow mass movements in south-central British Columbia: the influence of hydroclimatic changes: Canadian Journal of Earth Sciences, v. 29, p. 1746–1755, doi: 10.1139/e92-137.

Brown, W.M., and Ritter, J.R., 1971, Sediment transport and turbidity in the Eel River basin, California: USGS Water Supply Paper 1986.: Washington D.C.

Chapuis, R. P. (2012). Predicting the saturated hydraulic conductivity of soils: A review. Bulletin of Engineering Geology and the Environment, 71(3), 401–434. https://doi.org/10.1007/s10064-012-0418-7

Chapuis, R. P., & Aubertin, M. (2003). On the use of the Kozeny – Carman equation to predict the hydraulic conductivity of soils. Canadian Geotechnical Journal, 628(1927), 616–628. https://doi.org/10.1139/T03-013

Clevers, J. G. P. W. (1988). The derivation of a simplified reflectance model for the estimation of leaf area index. Remote Sensing of Environment, 25(1), 53–69. https://doi.org/10.1016/0034-4257(88)90041-7

Coe, J.A., 2012, Regional moisture balance control of landslide motion: Implications for landslide forecasting in a changing climate: Geology, v. 40, p. 323–326, doi: 10.1130/G32897.1.

Coe, J.A., Ellis, W., Godt, J., Savage, W., Savage, J., Michael, J., Kibler, J., Powers, P., Lidke, D., and Debray, S., 2003, Seasonal movement of the Slumgullion landslide determined from Global Positioning System surveys and field instrumentation, July 1998–March 2002: Engineering Geology, v. 68, p. 67–101, doi: 10.1016/S0013-7952(02)00199-0.

Coe, J.A., McKenna, J.P., Godt, J.W., and Baum, R.L., 2009, Basal-topographic control of stationary ponds on a continuously moving landslide, Earth Surface Processes and Landforms, v. 34, p. 264-279, doi: 10.1002/esp.1721.

Cohen-Waeber, J., Bürgmann, R., Chaussard, E., Giannico, C., and Ferretti, A., 2018, Spatiotemporal Patterns of Precipitation-Modulated Landslide Deformation From Independent Component Analysis of InSAR Time Series: Geophysical Research Letters, v. 45, p. 1878–1887, doi: 10.1002/2017GL075950.

Contreras, I. a., Grosser, A.T., Ver Strate, R.H., and Strate, R.H., 2008, The use of the fully-grouted method for piezometer installation Part 1 and Part 2: Geotechnical Instrumentation News, v. 26, p. 30–37.

Cornforth, D. H. (2005). Landslides in Practice: Investigation, Analysis, and Remedial/Preventative Options in Soils. Hoboken, NJ: John Wiley & Sons, Inc.

Crandell, D.R., and Varnes, D.J., 1961, Movement of the Slumgullion earthflow near Lake City, Colorado, U.S. Geological Survey Research: U.S. Geological Survey Professional Paper 424-B.:

Dai, A., and National Center for Atmospheric Research Staff, 2017, The Climate Data Guide: Palmer Drought Severity Index (PDSI): https://climatedataguide.ucar.edu/climate-data/palmer-drought-severity-index-pdsi (accessed November 2017).

Daly, C., Gibson, W.P., Taylor, G.H., Johnson, G.L., and Pasteris, P., 2002, A knowledge-based approach to the statistical mapping of climate: Climate Research, v. 22, p. 99–113, doi: 10.3354/cr022099.

Davila Olivera, S., Nereson, A.L., and Finnegan, N.J., 2017, Soil Properties and the Conditions for Recurring Earthflow Failure: Abstract presented at 2017 Fall Meeting, AGU, New Orleans, Louisiana, 11-15 December.

Del Soldato, M., Riquelme, A., Bianchini, S., Tomàs, R., Di Martire, D., de Vita, P., et al. (2018). Multisource data integration to investigate one century of evolution for the Agnone landslide (Molise, southern Italy). Landslides, 1–16. https://doi.org/10.1007/s10346-018-1015-z

Department, S.F.P., 2008, Final Program Environmental Impact Report on the San Francisco Public Utilities Commission's Water System Improvement Program. State Clearinghouse No. 2005092026:

Dibblee, T.W., and Minch, J.A., 2005, Geologic map of the Calaveras Reservoir quadrangle, Alameda and Santa Clara counties, California, scale 1:24:000.

Dibblee, T. W., & Minch, J. A. (2006). Geologic map of the Mount Day quadrangle, Santa Clara & Alameda counties, California. Santa Barbara: Santa Barbara Museum of Natural History.

Fetter, C.W., 2001, Applied Hydrology: Upper Saddle River, NJ, Prentice-Hall, Inc., 598 p.

Finnegan, N.J. & Nereson, A.L. (2017). Untangling Topographic and Climatic Forcing of Earthflow Motion. Paper presented at American Geophysical Union Annual Fall Meeting, New Orleans, LA.

Fleming, R.W., and Taylor, F.A., 1980, Estimating the costs of landslide damage in the United States: Geological Survey Circular 832, p. 21.

Fleming, R.W., Baum, R.L., and Giardino, M., 1999, Map and description of the active part of the Slumgullion landslide, Hinsdale County, Colorado: United States Geological Survey, Geological Investigations Series Map I-2672.

Freeze, R.A., and Cherry, J.A., 1979, Groundwater: Englewood Cliffs, NJ, Prentice-Hall, Inc., 604 p.

Gao, Z., Xu, X., Wang, J., Yang, H., Huang, W., & Feng, H. (2013). A method of estimating soil moisture based on the linear decomposition of mixture pixels. Mathematical and Computer Modelling, 58(3–4), 606–613. https://doi.org/10.1016/j.mcm.2011.10.054

Gillham, R.W., 1984, The capillary fringe and its effect on water-table response: Journal of Hydrology, v. 67, p. 307–324, doi: 10.1016/0022-1694(84)90248-8.

Griffin, D., and Anchukaitis, K.J., 2014, How unusual is the 2012-2014 California drought? Geophysical Research Letters, v. 41, p. 9017–9023, doi: 10.1002/2014GL062433.

Graymer, R. W., Moring, B. C., Saucedo, G. J., Wentworth, C. M., Brabb, E. E., & Knudsen, K. L. (2006). Geologic map of the San Francisco Bay region. Scientific Investigations Map. Reston, VA. Retrieved from http://pubs.er.usgs.gov/publication/sim2918

Guerriero, L., Coe, J.A., Revellino, P., Grelle, G., Pinto, F., and Guadagno, F.M., 2014, Influence of slip-surface geometry on earth-flow deformation, Montaguto earth flow, southern Italy: Geomorphology, v. 219, p. 285–305, doi: 10.1016/j.geomorph.2014.04.039.

Guerriero, L., Revellino, P., Bertello, L., Grelle, G., Berti, M., and Maria Guadagno, F., 2016, Kinematic Segmentation and Velocity in Earth Flows: A Consequence of Complex Basal-slip Surfaces: Procedia Earth and Planetary Science, v. 16, p. 146–155, doi: 10.1016/J.PROEPS.2016.10.016.

Handwerger, A.L., Roering, J.J., and Schmidt, D. a., 2013, Controls on the seasonal deformation of slow-moving landslides: Earth and Planetary Science Letters, v. 377–378, p. 239–247, doi: 10.1016/j.epsl.2013.06.047.

Haneberg, W.C., 1991, Pore Pressure Diffusion and the Hydrologic Response of Nearly Saturated, Thin Landslide Deposits to Rainfall: Journal of Geology, v. 99, p. 886–892.

Hilley, G.E., Burgmann, R., Ferretti, A., Novali, F., and Rocca, F., 2004, Dynamics of Slow-Moving Landslides from Permanent Scatterer Analysis: Science, v. 304, p. 1952–1955.

Hungr, O., Leroueil, S., and Picarelli, L., 2014, The Varnes classification of landslide types, an update: Landslides, v. 11, p. 167–194, doi: 10.1007/s10346-013-0436-y.

Iverson, R.M., 1986a, Unsteady, Nonuniform Landslide Motion: 1. Theoretical Dynamics and the Steady Datum State: The Journal of Geology, v. 94, p. 1–15.

Iverson, R.M., 1986b, Unsteady, Nonuniform Landslide Motion: 2 . Linearized Theory and the Kinematics of Transient Response: The Journal of Geology, v. 94, p. 349–364.

Iverson, R. M. (2000). Acute Sensitivity of Landslide Rates to Initial Soil Porosity. Science, 290(5491), 513–516. https://doi.org/10.1126/science.290.5491.513

Iverson, R.M., 2000, Landslide triggering by rain infiltration: Water Resources Research, v. 36, p. 1897, doi: 10.1029/2000WR900090.

Iverson, R.M., 2005, Regulation of landslide motion by dilatancy and pore pressure feedback: Journal of Geophysical Research, v. 110, p. F02015, doi: 10.1029/2004JF000268.

Iverson, R., and Major, J., 1987, Rainfall, ground-water flow, and seasonal movement at Minor Creek landslide, northwestern California: Physical interpretation of empirical relations: Geological Society of America Bulletin, v. 99, p. 579–594.

Jacobi, J., Perrone, D., Duncan, L.L., and Hornberger, G., 2013, A tool for calculating the Palmer drought indices: Water Resources Research, v. 49, p. 6086–6089, doi: 10.1002/wrcr.20342.

Jensen, J. R. (2007). Remote sensing of the environment: an earth resource perspective. (K. C. Clarke, Ed.) (2nd ed.). Upper Saddle River.

Kauffman, E., 2003, Climate and Topography, in California Dept. of Fish and Game ed., Atlas of the biodiversity of California, California Department of Fish and Game, p. 12–15.

Keefer, D., and Johnson, A., 1983, Earth flows: morphology, mobilization, and movement: Washington D.C., U.S. Government Printing Office.

Kelsey, H.M., 1978, Earthflows in Franciscan melange, Van Duzen River basin, California: Geology, v. 6, p. 361–364.

Korup, O., Densmore, A.L., and Schlunegger, F., 2010, The role of landslides in mountain range evolution: Geomorphology, v. 120, p. 77–90, doi: 10.1016/j.geomorph.2009.09.017.

Lambe, T.W., and Whitman, R.V., 1969, Soil Mechanics: New York, Wiley.

Liu, S., Chadwick, O. a., Roberts, D. a., & Still, C. J. (2011). Relationships between GPP, Satellite Measures of Greenness and Canopy Water Content with Soil Moisture in Mediterranean-Climate Grassland and Oak Savanna. Applied and Environmental Soil Science, 2011, 1–14. https://doi.org/10.1155/2011/839028

Liu, Y., Hill, M. J., Zhang, X., Wang, Z., Richardson, A. D., Hufkens, K., et al. (2017). Using data from Landsat, MODIS, VIIRS and PhenoCams to monitor the phenology of California oak/grass savanna and open grassland across spatial scales. Agricultural and Forest Meteorology, 237–238, 311–325. https://doi.org/10.1016/j.agrformet.2017.02.026

Mackey, B.H., and Roering, J.J., 2011, Sediment yield, spatial characteristics, and the long-term evolution of active earthflows determined from airborne LiDAR and historical aerial photographs, Eel River, California: Geological Society of America Bulletin, v. 123, p. 1560–1576, doi: 10.1130/B30306.1.

Mackey, B.H., Roering, J.J., and McKean, J. a., 2009, Long-term kinematics and sediment flux of an active earthflow, Eel River, California: Geology, v. 37, p. 803–806, doi: 10.1130/G30136A.1.

Madole, R.F., 1996, Preliminary chronology of the Slumgullion landslide, Hinsdale County, Colorado, in J, V.D. and Z, S.W. eds., The Slumgullion earth flow--a large-scale natural laboratory: U.S. Geological Survey Bulletin 2130, p. 5–7.

McKean, J.A., 1993, Soil creep and earthflows: geomorphic analysis using cosmogenic isotopes and remote sensing [Ph.D. Thesis]: Berkeley, University of California, 264 p.

McKean, J., Buechel, S., & Gaydos, L. (1991). Remote Sensing and Landslide Hazard Assessment. Photogrammetric Engineering & Remote Sensing, 57(9), 1185–1193. Retrieved from https://www.asprs.org/wp-content/uploads/pers/1991journal/sep/1991_sep_1185-1193.pdf

McSaveney, M.J., and Griffiths, G.A., 1987, Drought, rain, and movement of a recurrent earthflow complex in New Zealand: Geology, v. 15, p. 643–646, doi: 10.1080/00480169.1972.34028.

Murphy, C., and Finnegan, N., 2018, Evidence for a Positive Feedback Between Shallow Groundwater Flow and Shear Failure in an Active Earthflow, in American Geophysical Union Annual Fall Meeting,.

Nereson, A.L., and Finnegan, N.J., 2018, Drivers of earthflow motion revealed by an eighty year record of displacement from Oak Ridge earthflow, Diablo Range, California, USA (in press): Geological Society of America Bulletin.

Nereson, A.L., Finnegan, N.J., and Booth, A.M., 2013, Evaluating controls on the aspect dependence of earthflows in the central California Coast Ranges: Abstract presented at 2013 Fall Meeting, AGU, 9-13 December.

Parise, M., Moscariello, A., and Fleming, R.W., 1997, Evidence from flank ridges for long-term diminishing movements of the Slumgullion landslide, Hinsdale County, Colorado, U.S. Geological Survey Open-File Report 97-517, 14 p.

Petley, D., 2012, Global patterns of loss of life from landslides: Geology, v. 40, p. 927–930, doi: 10.1130/G33217.1.

Picarelli, L., Urciuoli, G., and Russo, C., 2004, Effect of groundwater regime on the behaviour of clayey slopes: Canadian Geotechnical Journal, v. 41, p. 467–484, doi: 10.1139/t04-009.

Planet Team (2018). Planet Application Program Interface: In space for life on Earth. San Francisco, CA. Retrieved from https://api.planet.com

PRISM Climate Group, Oregon State University, http://prism.oregonstate.edu , created 1 Aug 2017

Qi, J., Chehbouni, A., Huete, A. R., Kerr, Y. H., & Sorooshian, S. (1994). A modified soil adjusted vegetation index. Remote Sensing of Environment, 48(2), 119–126. https://doi.org/10.1016/0034-4257(94)90134-1

Reid, M.E., 1994, A Pore-Pressure Diffusion Model for Estimating Landslide-Inducing Rainfall: Journal of Geology, v. 102, p. 709–717.

Robeson, S. M. (2015). Revisiting the recent California drought as an extreme value. Geophysical Research Letters, 42(16), 6771–6779. https://doi.org/10.1002/2015GL064593

Roering, J.J., Mackey, B.H., Handwerger, A.L., Booth, A.M., Schmidt, D. a., Bennett, G.L., and Cerovski-Darriau, C., 2015, Beyond the angle of repose: A review and synthesis of landslide processes in response to rapid uplift, Eel River, northern California: Geomorphology, v. 236, p. 109–131.

Rubin, R.S., 2002, Franciscan Complex geology northeast of Calaveras Reservoir, Diablo Range, California: San Jose State University, 137 p.

Savage, W., & Wasowski, J. (2006). A plastic flow model for the Acquara - Vadoncello landslide in Senerchia, Southern Italy. Engineering Geology, 83(1–3), 4–21. https://doi.org/10.1016/j.enggeo.2005.06.024

Scheingross, J.S., Minchew, B.M., Mackey, B.H., Simons, M., Lamb, M.P., and Hensley, S., 2013, Fault-zone controls on the spatial distribution of slow-moving landslides: Geological Society of America Bulletin, v. 125, p. 473–489, doi: 10.1130/B30719.1.

Schulz, W.H., Kean, J.W., and Wang, G., 2009, Landslide movement in southwest Colorado triggered by atmospheric tides: Nature Geoscience, v. 2, p. 863–866, doi: 10.1038/ngeo659.

Schulz, W.H., McKenna, J.P., Kibler, J.D., and Biavati, G., 2009, Relations between hydrology and velocity of a continuously moving landslide-evidence of pore-pressure feedback regulating landslide motion? Landslides, v. 6, p. 181–190, doi: 10.1007/s10346-009-0157-4.

Schulz, W.H., Smith, J.B., Wang, G., Jiang, Y., and Roering, J.J., 2018, Clayey Landslide Initiation and Acceleration Strongly Modulated by Soil Swelling: Geophysical Research Letters, v. 45, p. 1888–1896, doi: 10.1002/2017GL076807.

Shahzad, Z., Canut, M., Tournaire-Roux, C., Martinière, A., Boursiac, Y., Loudet, O., & Maurel, C. (2016). A Potassium-Dependent Oxygen Sensing Pathway Regulates Plant Root Hydraulics. Cell, 167(1), 87–98. https://doi.org/10.1016/j.cell.2016.08.068

Simoni, A., Ponza, A., Picotti, V., Berti, M., and Dinelli, E., 2013, Earthflow sediment production and Holocene sediment record in a large Apennine catchment: Geomorphology, v. 188, p. 42–53, doi: 10.1016/J.GEOMORPH.2012.12.006.

Skempton, A. W., & Petley, D. J. (1967). The Strength along Structural Discontinuities in Stiff Clays. Proceedings of the Geotechincal Conference, Oslo, (2), 29–46. https://doi.org/10.1680/sposm.02050.0018

Del Soldato, M., Riquelme, A., Bianchini, S., Tomàs, R., Di Martire, D., de Vita, P., Moretti, S., and Calcaterra, D., 2018, Multisource data integration to investigate one century of evolution for the Agnone landslide (Molise, southern Italy): Landslides, p. 1–16, doi: 10.1007/s10346-018-1015-z.

Sorensen, K. K., & Okkels, N. (2013). Correlation between drained shear strength and plasticity index of undisturbed overconsolidated clays Corrélation entre la résistance au cisaillement des sols drainés et l ' indice de plasticité des argiles surconsolidés non perturbées. In Proceedings of the 18th International Conference on Soil Mechanics and Geotechnical Engineering (pp. 423–428). Paris.

Stark, T. D., & Hussain, M. (2013). Empirical Correlations: Drained Shear Strength for Slope Stability Analyses. Journal of Geotechnical and Geoenvironmental Engineering, (June), 853–862. https://doi.org/10.1061/(ASCE)GT.1943-5606.0000824

Terzaghi, K., 1950, Mechanism of Landslides, in Paige, S. ed., Application of Geology to Engineering Practice, Geological Society of America, p. 83–123.

Terzaghi, K., Peck, R. B., & Mesri, G. (1996). Soil Mechanics in engineering practice.

USDA Natural Resources Conservation Service, 1998, Soil Quality Resource Concerns: Available Water Capacity: https://www.nrcs.usda.gov/Internet/FSE_DOCUMENTS/nrcs142p2_051279.pdf (accessed October 2017).

Vallet, A., Bertrand, C., Fabbri, O., and Mudry, J., 2015, An efficient workflow to accurately compute groundwater recharge for the study of rainfall-triggered deep-seated landslides, application to the Séchilienne unstable slope (western Alps): Hydrology and Earth System Sciences, v. 19, p. 427–449, doi: 10.5194/hess-19-427-2015.

Van Asch, T.W.J., 2005, Modelling the hysteresis in the velocity pattern of slow-moving earth flows: The role of excess pore pressure: Earth Surface Processes and Landforms, v. 30, p. 403–411, doi: 10.1002/esp.1147.

Vulliet, L., and Hutter, K., 1988, Viscous-type sliding laws for landslides: Canadian Geotechnical Journal, v. 25, p. 467–477, doi: 10.1139/t88-052.

Wakabayashi, J., 1992, Nappes, Tectonics of Oblique Plate Convergence, and Metamorphic Evolution Related to 140 Million Years of Continuous Subduction, Franciscan Complex, California: The Journal of Geology, v. 100, p. 19–40, doi: 10.1086/629569.

Wiegers, M.O., 2011, Landslide Inventory Map of the Calaveras Reservoir Quadrangle, Alameda and Santa Clara Counties, California: California Geological Survey, scale 1:24,000.

Wiegand, C. L., & Richardson, A. J. (1982). Comparisons among a new soil index and other two- and four-dimensional vegetation indices. In Proceedings of the 48th Annual Meeting, American Society of Photogrammetry (pp. 211–227).

Wolter, K., and Timlin, M.S., 1998, Measuring the strength of ENSO events: How does 1997/98 rank? Weather, v. 53, p. 315–324, doi: 10.1002/j.1477-8696.1998.tb06408.x.

Zhang, X., Phillips, C., and Marden, M., 1991, Internal deformation of a fast-moving earthflow, Raukumara Peninsula, New Zealand: Geomorphology, v. 4, p. 145–154, doi: 10.1016/016